Article

Neuron

Distinct Cortical-Thalamic-Striatal Circuits through the Parafascicular Nucleus

Graphical Abstract

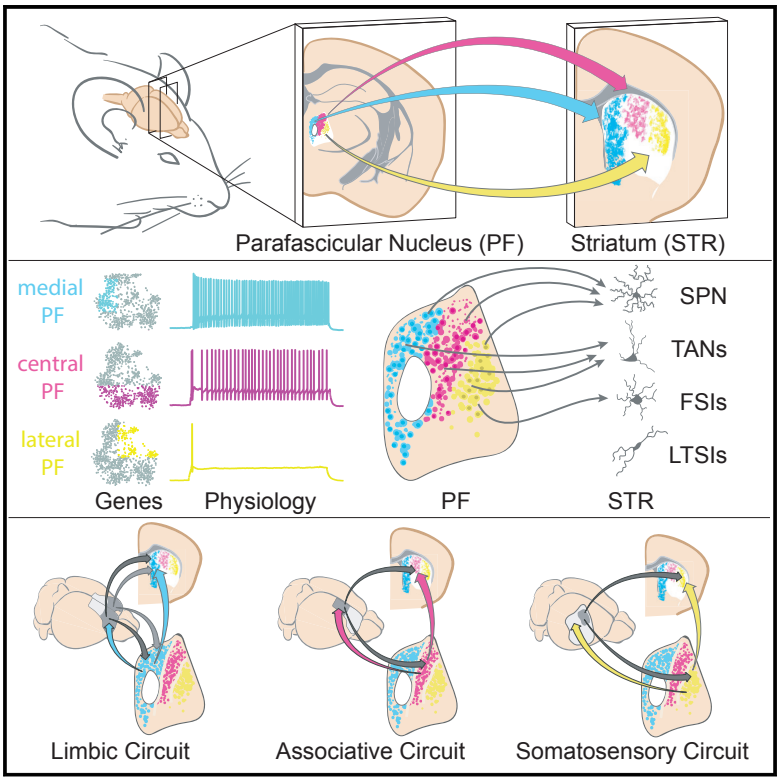

Highlights

- Mouse PF has the highest density of striatum-projecting neurons in subcortex
- In PF, neurons are anatomically, transcriptionally, and physiologically organized
- Cortical-PF-cortical and cortical-PF-striatum circuit motifs are revealed
- PF is organized as parallel and independent limbic, associative, and somatosensory circuits

Authors

Gil Mandelbaum, Julian Taranda, Trevor M. Haynes, ..., Keiramarie Robertson, Pavel Osten, Bernardo L. Sabatini

Correspondence

bsabatini@hms.harvard.edu

In Brief

The PF of the intralaminar thalamus is implicated in human neuropsychiatric disease. Mandelbaum et al. deconstruct the mouse PF using transcription, electrophysiological, and whole-brain anatomical analyses. They reveal organization of the PF that bridges molecular, cellular, and circuit levels, forming cortical-PF-cortical and cortical-PF-striatum circuit motifs. These findings reveal PF as a critical node that organizes limbic, associative, and somatosensory information in the basal ganglia.

Mandelbaum et al., 2019, Neuron *102*, 1–17
May 8, 2019
https://doi.org/10.1016/j.neuron.2019.02.035

CellPress

Please cite this article in press as: Mandelbaum et al., Distinct Cortical-Thalamic-Striatal Circuits through the Parafascicular Nucleus, Neuron (2019), https://doi.org/10.1016/j.neuron.2019.02.035

Neuron
Article

CellPress

Distinct Cortical-Thalamic-Striatal Circuits through the Parafascicular Nucleus

Gil Mandelbaum,[1] Julian Taranda,[2] Trevor M. Haynes,[1] Daniel R. Hochbaum,[1,3] Kee Wui Huang,[1] Minsuk Hyun,[1] Kannan Umadevi Venkataraju,[2] Christoph Straub,[1] Wengang Wang,[1] Keiramarie Robertson,[1] Pavel Osten,[2] and Bernardo L. Sabatini[1,4,*]

[1]Howard Hughes Medical Institute, Department of Neurobiology, Harvard Medical School, Boston, MA 02115, USA
[2]Cold Spring Harbor Laboratory, Cold Spring Harbor, NY 11724, USA
[3]Society of Fellows, Harvard University, Cambridge, MA 02138, USA
[4]Lead Contact
*Correspondence: bsabatini@hms.harvard.edu
https://doi.org/10.1016/j.neuron.2019.02.035

SUMMARY

The thalamic parafascicular nucleus (PF), an excitatory input to the basal ganglia, is targeted with deep-brain stimulation to alleviate a range of neuropsychiatric symptoms. Furthermore, PF lesions disrupt the execution of correct motor actions in uncertain environments. Nevertheless, the circuitry of the PF and its contribution to action selection are poorly understood. We find that, in mice, PF has the highest density of striatum-projecting neurons among all sub-cortical structures. This projection arises from transcriptionally and physiologically distinct classes of PF neurons that are also reciprocally connected with functionally distinct cortical regions, differentially innervate striatal neurons, and are not synaptically connected in PF. Thus, mouse PF contains heterogeneous neurons that are organized into parallel and independent associative, limbic, and somatosensory circuits. Furthermore, these subcircuits share motifs of cortical-PF-cortical and cortical-PF-striatum organization that allow each PF subregion, via its precise connectivity with cortex, to coordinate diverse inputs to striatum.

INTRODUCTION

Selecting and generating appropriate motor actions requires integration of limbic, associative, and sensory information in the basal ganglia (BG) (Macpherson et al., 2014; Hintiryan et al., 2016; Hooks et al., 2018), a set of phylogenetically old subcortical nuclei (Stephenson-Jones et al., 2011). The importance of these nuclei to action selection in humans is emphasized by disorders with disrupted BG function, such as Parkinson's and Huntington's diseases (Nelson and Kreitzer, 2014).

The BG consist of loops formed by projections from cortex (CTX) and thalamus (TH) to the input stage of the BG, the striatum (STR), which signals via cascading inhibitory nuclei to cortically projecting thalamic nuclei (Cowan and Powell, 1956; DeLong, 1990; Nelson and Kreitzer, 2014). Phylogenetically, TH and the STR pre-date the expansion of the CTX (Reiner et al., 1998) and, despite TH being approximately ten times smaller in volume than CTX in mice, it accounts for approximately a quarter of all glutamatergic synapses in STR (Huerta-Ocampo et al., 2014). This suggests that evolutionally conserved projections between TH and STR have a powerful functional impact on BG circuits (Minamimoto et al., 2005; Bradfield et al., 2013).

Within TH, the neighboring parafascicular (PF) and centromedian (CM) nuclei project heavily to STR (Smith and Parent, 1986; Berendse and Groenewegen, 1990; Wall et al., 2013), unlike typical thalamic nuclei that primarily interact with CTX (Sherman and Guillery, 2013). In humans, targeting PF/CM for deep-brain stimulation (DBS) can alleviate symptoms in individuals with BG-related disorders (Peppe et al., 2008; Testini et al., 2016). Furthermore, PF/CM degenerate early in Parkinson's disease, unlike other thalamic nuclei that maintain their integrity throughout the disease (Henderson et al., 2000). However, the PF/CM is often omitted from models of both primate and rodent BG (Penney and Young, 1983; DeLong, 1990; Nelson and Kreitzer, 2014) or are grouped with other thalamostriatal projections, despite evidence that their anatomy and function are specialized (Ellender et al., 2013; Alloway et al., 2014).

In primates, projections from PF/CM to STR are anatomically organized into multiple functionally distinct output channels (Steiner and Tseng, 2016; Sadikot and Rymar, 2009), a finding that seems to grossly hold in cats and rats (Giménez-Amaya et al., 2000; Jones, 2007). However, understanding the polysynaptic nature of circuits across nuclei in genetically intractable species is challenging. Therefore, it has not been possible to map the distinct projections from subregions of PF/CM to specific cell classes or to understand their relationship with cortical regions that project to STR and TH. Furthermore, the difficulty of genetic manipulations and *ex vivo* electrophysiology analysis in these species limits studies of the cellular composition and micro-circuitry of PF/CM, the neurons that comprise their input and output channels, and synapses by which PF/CM modulate STR activity. Conversely, in rodents, the lack of histological demarcations within and between PF and CM as well as the small size and close packing of TH nuclei have led researchers to treat mouse PF as anatomically uniform and cellularly homogeneous (Parker et al., 2016; Kato et al.,

2011; Aceves Buendia et al., 2017; Assous et al., 2017; Choi et al., 2018).

Here, we deconstruct the mouse PF. Using quantitative anatomical approaches, we reveal that PF has the highest density of striatum-projecting neurons among sub-cortical structures. We find that PF contains anatomically, transcriptionally, and physiologically distinct neuronal populations with topographically organized projections to STR and to and from CTX. Each PF subregion and neuron class influences distinct striatal regions and cell classes through independent and parallel channels that carry information principally from limbic, associative, or somatosensory cortical regions. These channels are organized such that an area of STR receives input from regions of CTX and PF that are themselves reciprocally interconnected. We propose that PF circuits facilitate and dynamically shape the output of connected and behaviorally relevant striatal regions to mediate correct action selection in the ongoing sensorimotor context.

RESULTS

Mapping the Distribution of Inputs to Striatum across the Brain

Inputs from a few dozen brain regions to STR (Steiner and Tseng, 2016) have been mapped and quantified using retrograde tracing and manual cell counting (Wall et al., 2013). Alternatively, anterograde tracing was combined with image analysis to define striatal regions by the combinations of inputs received from CTX and TH (Hunnicutt et al., 2016; Hintiryan et al., 2016; Hooks et al., 2018).

We utilized automated image acquisition and analysis to map the distribution of putative STR-projecting neurons across the brain (Figure 1; Video S1). We injected 4 locations in the STR of C57BL6/N wild-type (WT) mice with a non-pseudotyped rabies virus encoding nuclear localized GFP (RV-nGFP) (Figure 1A). The 3D brain volume was subsequently imaged, reconstructed, and aligned to the Allen Brain Atlas (ABA) (Figure 1A). We adopted the brain-structure hierarchy and abbreviations defined in ABA with the exception that, instead of referring to sub-cortical structures as brain stem, we refer to them as sub-cortical (sub-CTX) (Table S1 for abbreviations).

The high signal-to-noise ratio (SNR) of nuclear GFP signal was exploited to automatically count RV-nGFP+ cells (Figure 1B), permitting an unbiased estimate of putative inputs to STR from hundreds of brain structures (Video S1). The coefficients of variation (CVs) of the volumes of interest across mice were less than 4% (Figures S1A–S1C), allowing pooling of data across brains. The false positive rate (FPR) for detection of RV-nGFP+ cells was estimated from cell counts in the STR and PF contralateral (CONTRA) to the injection site, as there is no PF→STR or STR→STR connectivity across hemispheres. This yielded an estimate of <1% FPR (ipsilateral [IPSI]: STR = 23,396 ± 2,332 cells, PF = 6,797 ± 81; CONTRA: STR = 229 ± 42, PF = 51 ± 1; n = 7 mice; Figure S1D). Furthermore, in a subset of mice, labeled PF neurons were counted manually, yielding similar numbers (3,219 ± 80 cells) to the automated measurements (3,375 ± 48; n = 3 mice; Figure 1C).

To investigate the distribution of inputs to STR in the sub-CTX main hierarchical divisions, the % of the total RV-nGFP+ cells located in each group was calculated. TH had the highest percentage (48% ± 1%), with the motor region of the midbrain (MOT) being second (16% ± 1%). The other 7 sub-CTX groups together had 35% of labeled cells (Figure 1D; Table S2.1 for full dataset). In TH, the majority of nGFP+ cells were in the poly-modal association cortex-related region (DORpm 79% ± 0.6%) and not the sensory-motor cortex-related region (DORsm 10% ± 0%; Figures 1E and 1F). Among DORsm nuclei, the ventral anterior lateral complex had the most cells (Figure S1E), similar to previous observations in the squirrel monkey (Smith and Parent, 1986).

In DORpm, the intralaminar (ILM) thalamic nuclei group had the majority of putative STR inputs (43% ± 3%), with PF having the highest percent of nGFP+ cells compared to all other ILM nuclei (68% ± 1%; Figures 1G and 1H). Lastly, the density of putative inputs to STR (defined as % of total nGFP+ cells in a region divided by its volume) was calculated for the 706 ABA-defined substructures—PF had the highest density of STR-projecting neurons among all sub-CTX structures, highlighting its potential to exert powerful control over BG circuits.

Parafascicular-Striatal Projections Are Topographically Organized

In cats, primates, and humans, the PF/CM complex is separated into histologically dissimilar PF and CM nuclei, which are organized into multiple output channels with distinct targets (Jones, 2007; Steiner and Tseng, 2016). To address whether such topography exists in mice, 3 variants of the retrograde tracer cholera toxin subunit B (CTB) (Conte et al., 2009) were injected into 4 STR locations (Figures 2A and S2A). Topographically organized projections were observed in the anterior part of PF (coronal section −2.0 mm defined by the ABA as the anterior posterior border of PF with the medial dorsal nucleus) between medial PF (mPF) and medial STR (mSTR), central PF (cPF) and dorsal medial STR (dmSTR), and lateral PF (lPF) and dorsal lateral STR (dlSTR) (Figures 2B–2D). This topography was maintained at coronal section −2.1 and −2.2 mm but was less distinct at −2.3 mm, corresponding to the posterior PF (Figures 2E–2M).

The distribution of CTB-labeled PF→STR cells varies across the anterior-posterior axis of PF with decreasing labeling in posterior sections but is relatively uniform across the medial-lateral axis (Figure S2B). The distribution of CTB-labeled PF→STR cells differs for each PF→STR projection, showing a posterior bias for dmSTR-projecting neurons and anterior bias for dlSTR-projecting neurons (Figure S2C; Table S3). Little overlap was observed in PF between PF→STR CTB+ cells (Figure S2D; Table S3). Furthermore, the topography of projections from cPF→dmSTR was evident in cleared brains (Video S2; Chung et al., 2013). In addition, ventral mPF (v-mPF) projects to the nucleus accumbens shell, whereas cells medial to the fasciculus retroflexus (FR) project to the nucleus accumbens core (Figures S2E and S2F). Thus, despite its small size and lack of cytoarchitecturally evident substructure, mouse PF contains distinct and topographically organized projections to STR that share similar organizational features of PF and CM in larger species (Jones, 2007; Giménez-Amaya et al., 2000).

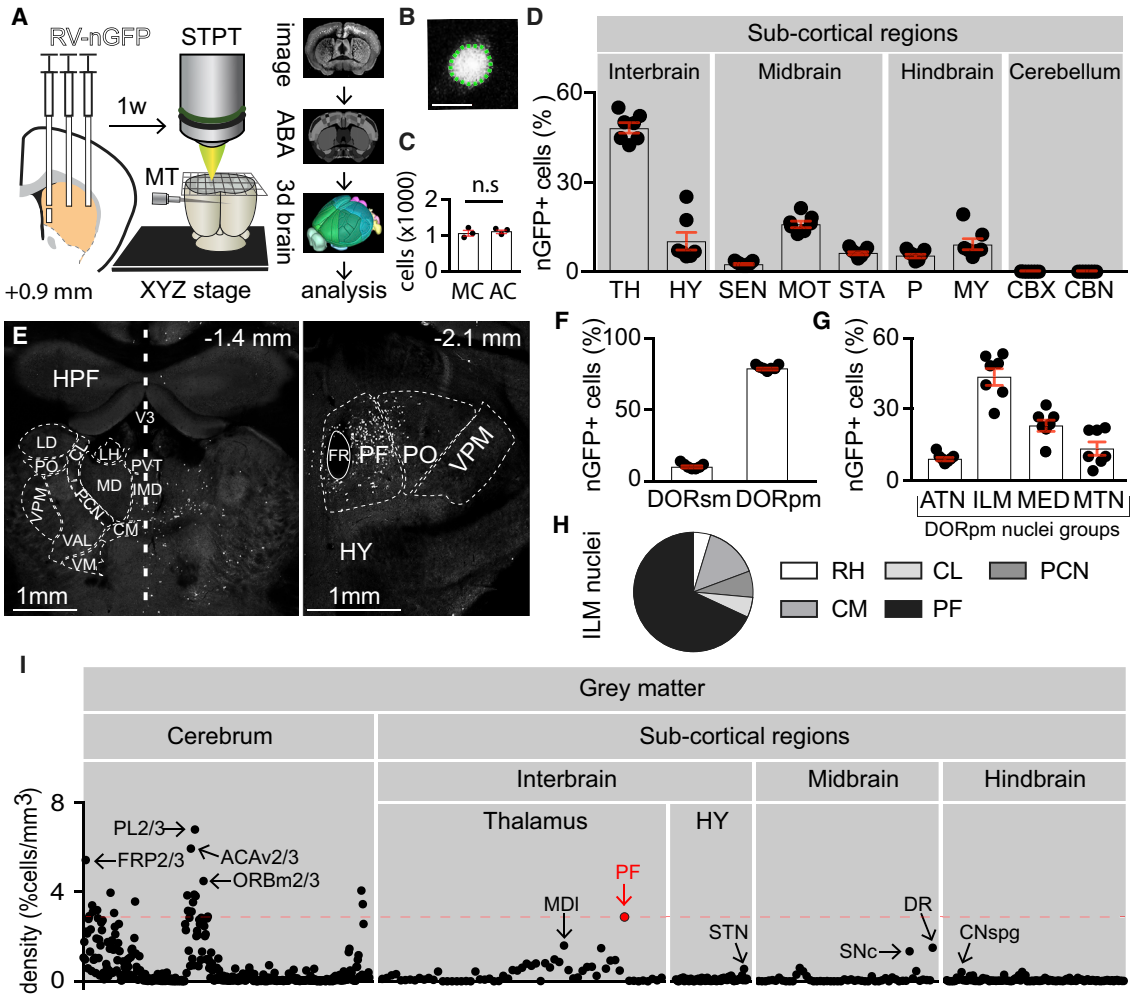

Figure 1. Serial Two-Photon Tomography Defines PF as the Main Sub-cortical Input to STR

(A) (Left) Schematic of the experimental design showing a coronal section at +0.9 mm from a mouse with 4 injections of RV-nGFP in STR (region of injection is highlighted in orange in all figures). (Middle) Schematic of STPT is shown, which automatically slices and images the whole brain using a microtome (MT) built into a 2-photon laser-scanning microscope. (Right) Image of a brain slice obtained approximately 1 week after virus injection that was aligned to the ABA and 3D reconstructed is shown.

(B) STPT image of the nucleus of a cell infected with RV-nGFP (white) with the border of nGFP marked (green line).

(C) Number of cells detected in PF by manual (MC) and automated (AC) counting (n = 3 mice). p = 0.5; Wilcoxon test. Red error bars in (C)–(I) indicate ± SEM, and black bar indicates the mean. In (C), (D), (F), and (G), each black circle indicates data from one mouse.

(D) Percentage of RV-nGFP+ cells in each indicated sub-CTX region for the experiment shown in (A) (n = 60,857/7 cells/mice).

(E) Coronal sections of TH at −1.4 (left) and −2.1 (right) mm showing RV-nGFP+ cells (white). On the left, boundaries of TH nuclei are shown with thin dashed lines CONTRA to the injection site in STR to not obscure the nGFP signal and the midline is indicated with a thick dashed line.

(F) Percentage of TH RV-nGFP+ cells found in sensory motor (DORsm) or poly-modal association (DORpm) cortex-related regions of TH (n = 26,490/7 cells/mice).

(G) Percentage of DORpm RV-nGFP+ cells found in 4 DORpm nuclei groups (n = 23,191/7 cells/mice).

(H) Pie chart of distribution of RV-nGFP+ cells across ILM TH nuclei (n = 10,019/7 cells/mice).

(I) Relative cell density (defined by % of total RV-nGFP+ cells in each brain region divided by its volume) for 706 regions. Each circle shows the mean density across mice (n = 7). Regions with high densities of RV-nGFP+ cells are labeled. PF is highlighted in red and has the highest density of putative projection neurons to STR in the sub-CTX (n = 668,890/7 cells/mice).

See related Figure S1, Table S2.1, and Video S1.

Transcriptional and Electrophysiological Analyses of PF Neurons

To examine the cellular heterogeneity in PF, we used droplet-based single-cell RNA sequencing (*inDrops*; Klein et al., 2015; Hrvatin et al., 2018; Figure 3). PF and its surrounding areas were manually dissected from acute brain slices, and a cell suspension was formed by tissue dissociation (Figure 3A). Analysis of transcriptomes of 10,471 cells from 8 mice revealed 7 main cell classes (Figure 3B). The neuronal class (enriched for *Snap25* and *Syn1*) contained 992 cells and expressed markers for glutamatergic (e.g., *Slc17a6*), but not GABAergic, neurotransmission (e.g., *Slc32a1*).

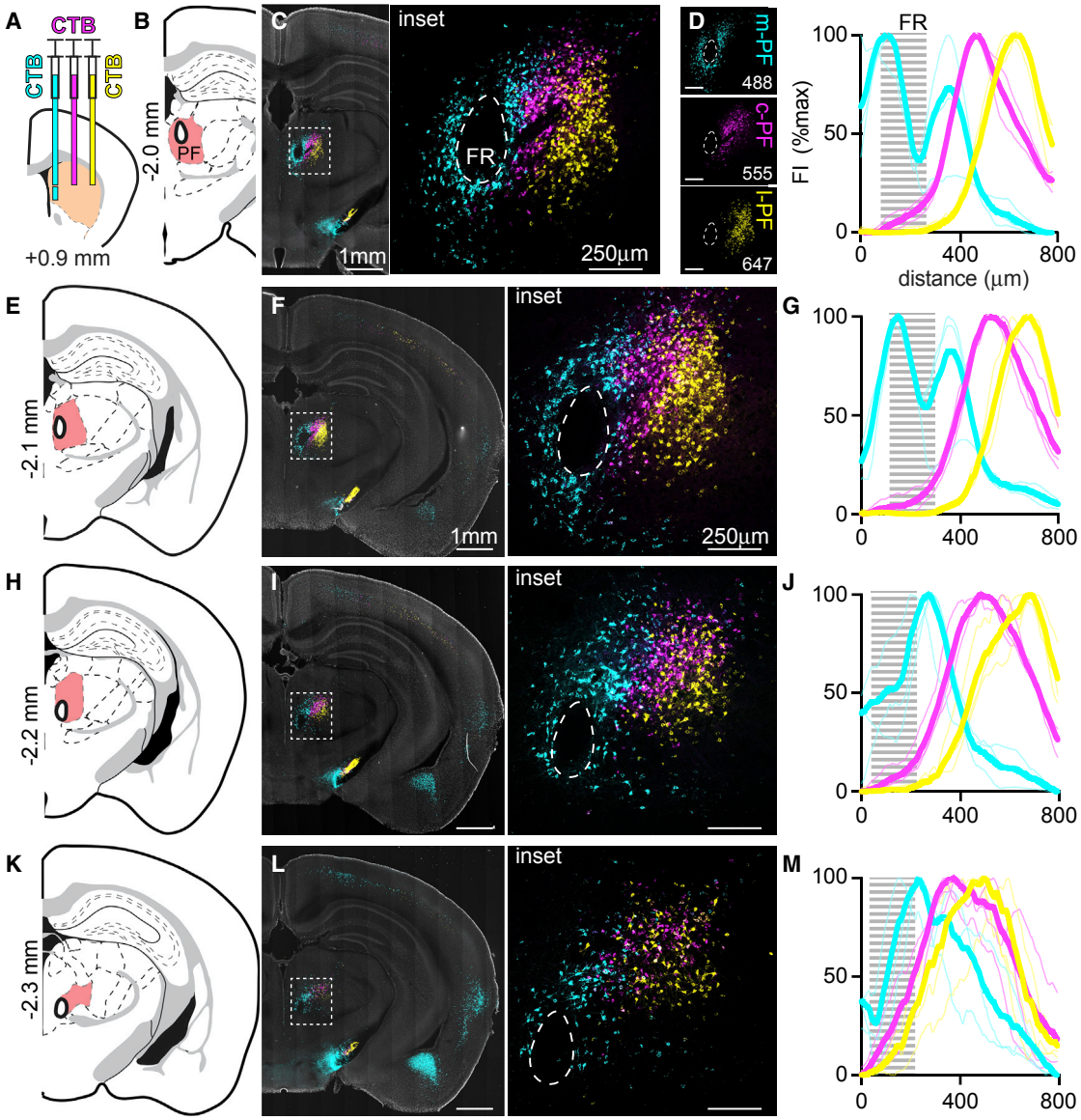

Figure 2. PF→STR Projections Are Topographically Organized

(A) Schematic of the experimental design showing a coronal section at +0.9 mm from a WT mouse with 4 injections of 3 CTB variants (cyan, magenta, and yellow) in the STR.

(B) Coronal section from the ABA at −2.0 mm with PF highlighted in red and the fasciculus retroflexus (FR) circled with a thick black line inside of PF. The FR was used as a landmark to align images across mice.

(C) Image of a coronal section at −2.0 mm (left) from the experiment shown in (A), with the inset indicating the region surrounding the PF enlarged on the right. The distributions of CTB conjugated with different fluorophores are largely not overlapping, highlighting the PF→STR topographical organization.

(D) (Left) Confocal images of PF excited with indicated wavelengths (top to bottom), highlighting the topographical organization of the PF-STR projections. (Right) Quantification of fluorescence intensity (FI) for each imaging channel along the medial-lateral axis at coronal section −2.0 mm is shown. Thin lines show peak-normalized data from individual mice and the thick lines the means for each channel (n = 3 mice). The gray region represents the FR. Scale bars represent 250 µm.

(E–G) Atlas schematics, images, and quantifications as in (B)–(D) for coronal section –2.1 mm.

(H–J) As in (E)–(G) but for coronal section –2.2 mm.

(K–M) As in (E)–(G) but for coronal section –2.3 mm.

See related Figure S2 and Video S2.

Sub-clustering of the neurons revealed 3 transcriptionally distinct subclasses (see STAR Methods; Figure 3C). Examination of the ABA *in situ* hybridization (ISH) database (ABA ISH: http://mouse.brain-map.org/; Lein et al., 2007) revealed that genes whose expression is elevated in cluster 1, including *Tnnt1*, are expressed outside of PF, primarily in posterior complex and the ventral posteromedial nucleus of TH (Figure 3D; Table S4.1; Phillips et al., 2018). Genes defining cluster 2, including

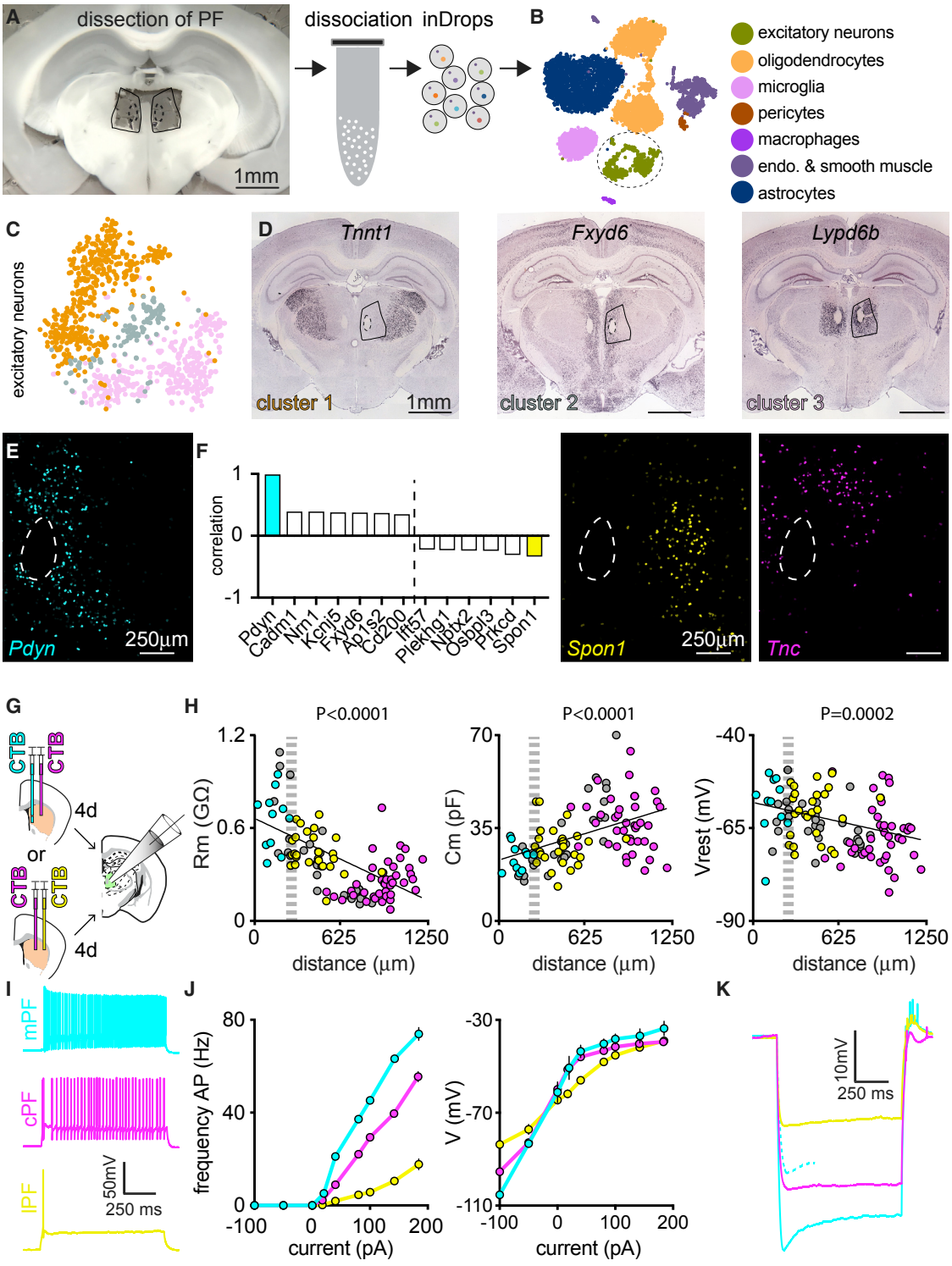

Figure 3. Transcriptional and Electrophysiological Characterization of PF Neurons

(A) (Left) Image of an acute coronal slice after microdissection of PF. (Right) Cell suspensions were formed from the dissected tissue and analyzed with *inDrops* to reveal single-cell transcriptomes.

(B) t-SNE plot showing the main identified cell types (n = 10,471/8 cells/mice) with excitatory neurons (green) delineated by the oval.

(C) t-Distributed stochastic neighbor embedding (t-SNE) plot of excitatory glutamatergic neurons (*Slc17a6* expressing) with the 3 subclusters indicated by different colors (n = 992/8 cells/mice).

(legend continued on next page)

Fxyd6, were expressed in mPF but also ventral and dorsal to the PF (Figure 3D; Table S4.2). Thus, cluster 1 and 2 represent neurons that, within the dissection area, are not unique to the PF.

Genes enriched in cluster 3, such as *Lypd6b*, showed specific expression in PF (Figure 3D; Table S4.3), including all of its subdivisions. Nevertheless, genes within cluster 3 were differentially expressed along the medial-lateral aspect of PF, indicating a heterogeneous neuronal population. For example, *Prodynorphin* (*Pdyn*) was expressed in 117 cells, with a mean 8-fold increase in expression compared to neuronal clusters 1 and 2. *ISH* of *Pdyn* mapped the expression specifically to mPF (Figure 3E). Furthermore, analysis of gene-gene expression correlation across all cells in cluster 3 (Table S4.4) revealed that those correlated with *Pdyn* also mapped to mPF (Figures 3F and S3A–S3C). Interestingly, given the degeneration of PF in individuals with Parkinson's, expression of *Snca* (encoding alpha-synuclein) is correlated with that of *Pdyn* (Table S4.4) and enriched in mPF (Figure S3D). Conversely, genes anti-correlated with *Pdyn* mapped to cPF and lPF (Figures 3F and S3E–S3G). Thus, anatomically defined subdomains of PF map onto transcriptionally distinct classes of neurons.

Recordings in primates revealed different kinetics of activation of PF and CM neurons (Matsumoto et al., 2001), whereas our transcriptional data indicate differential expression of ion channels across PF. Therefore, we examined whether the intrinsic electrophysiological properties of neurons projecting to the STR differ along the mediolateral aspect of PF. Whole-cell current-clamp recordings were obtained from CTB-labeled PF→STR neurons in acute brain slices from mice with different color CTBs injected into mSTR and dmSTR or dmSTR and dlSTR (Figure 3G). Indeed, the membrane resistance, capacitance, and resting potential varied across PF with higher input resistance, lower capacitance, and higher resting potential in neurons of mPF (Figure 3H). This suggests greater excitability of mPF compared to lPF neurons, consistent with higher firing rates observed *in vivo* in primates (Matsumoto et al., 2001). Injection of positive current resulted in higher action potential (AP) firing rates and higher membrane potential in mPF compared to cPF and lPF (Figures 3I and 3J; Table S4.5 for all the analyzed electrophysiological properties). Furthermore, mPF→mSTR neurons displayed a prominent "sag" in membrane potential in response to hyperpolarizing current injections (minimum and ending membrane potentials elicited by a −100 pA current pulse: mPF: −109.3 ± 2.5 and −101.3 ± 2.8 mV; cPF: −95.1 ± 2.0 and −95.4 ± 1.8; lPF: −87.9 ± 1.8 and −86.3 ± 1.6; Figure 3K). The selective presence of the sag in mPF neurons was not due to the more hyperpolarized potential reached, as it was also evoked with −50 pA current injection (Figure 3K). These findings may result from differences in expression of hyperpolarization-activated cyclic nucleotide-gated 1 (*Hcn1*), which underlies sag potentials (Robinson and Siegelbaum, 2003). Indeed, *Hcn1* was depleted from the cell cluster 1 but correlated with *Pdyn* in cluster 3 (Table S4.4).

Pdyn-Expressing Cells Are Located in mPF and Target the Matrix of STR

The restricted expression of *Pdyn* in PF and the existence of a well-characterized knockin mouse that expresses Cre recombinase from the *Pdyn* allele (*Pdyn-IRES-Cre*; Krashes et al., 2014) potentially permit specific manipulation of mPF circuitry. Indeed, *ISH* for *Pdyn* and *Slc17a6* confirmed that *Pdyn*+ PF cells are glutamatergic and localized to mPF (98% *Pdyn*+/*Slc17a6*+; n = 125/5/2 cells/slices/mice; Figures S4E and S4F). Injection of Cre-dependent adeno-associated virus (AAV) (CreOn-GFP) in PF of the adult *Pdyn-IRES-Cre* mice (Figure 4A) resulted in GFP expression restricted to mPF (Figures 4B, 4C, and S4A–S4D), including in the anterior-posterior axis of TH (% of cells anterior to, in, and posterior to PF: 6%, 90%, 3%; n = 2 mice; Figure 4D). mPF *Pdyn*+ cells target the medial band of STR (mSTR) and densely innervate STR neurons (Figures 4E–4H), and optogenetic stimulation of the Chr2-expressing *Pdyn*+ axons evoked excitatory postsynaptic currents (EPSCs) in SPNs in mSTR, but not dmSTR or dlSTR (fraction of SPNs with EPSCs: mSTR: 24/33; dmSTR: 0/7; dlSTR: 0/7; n = 4; mice; Figures 4G and 4H), verifying that the *Pdyn*+ cells in mPF innervate a specific region of the STR. The fluorophore-labeled axons of mPF *Pdyn*+ neurons were not uniform within mSTR, suggesting potential differential targeting of patch (striosome) and matrix (Herkenham and Pert, 1981). We found little overlap between GFP-labeled mPF axons in STR and regions expressing mu-opioid receptors (MOR), a marker of patches (Pert et al., 1976; Figure 4I). Indeed, the log ratio of fluorescence intensity (FI) inside of each patch divided by the FI of the "peri-patch" region (100 μm wide) surrounding each patch (Figure 4I) was consistently positive for the MOR channel and negative in the GFP-labeled mPF axon channel (log (FI patch/FI peri-patch) for the MOR channel = 0.14 ± 0.01 and GFP channel = –0.13 ± 0.00; n = 38/9/3 patches/slices/mice; Figure 4J), consistent with *Pdyn*+ mPF axons avoiding the MOR-rich STR compartments.

(D) *ISH* from the ABA for *Tnnt1* (cluster 1 and expressed in thalamus outside of PF), *Fxyd6* (cluster 2 and expressed in mPF and ventral dorsal to PF), and *Lypd6b* (cluster 3 and expressed throughout PF).
(E) *ISH* showing *Pdyn* expression in mPF.
(F) Multiple genes show significant correlation or anti-correlation with *Pdyn* expression on a cell-by-cell basis (left). This analysis reveals *Spon1* as being anti-correlated (yellow) with *Pdyn* and expressed in lPF (middle), whereas other genes, such as *Tnc*, are markers for cPF (right).
(G) Schematic of a coronal section at +0.9 mm depicting experimental configurations used to label neurons from mPF and cPF (top) or from cPF and lPF (bottom) that project to STR. 4 days after injections, whole-cell recordings were made in acute brain slices of PF (green).
(H) Intrinsic properties (membrane resistance [Rm], capacitance [Cm], and resting voltage [Vrest]) as a function of the location along the medial-lateral axis of the PF. The color indicates that of the CTB in the neuron (gray, unlabeled neurons). The FR is represented by the gray dashed area (n = 106/11 cells/mice).
(I) Voltage transients elicited by 1-s, 100-pA current injection in mPF (top, cyan), cPF (middle, magenta), and lPF (bottom, yellow) neurons.
(J) Frequency of evoked APs (left) and plateau potential (median voltage during the current injection; right) as functions of current amplitude for mPF (cyan), cPF (magenta), and lPF (yellow) neurons (n = 106/11 cells/mice).
(K) Mean voltage traces for mPF, cPF, and lPF neurons evoked by a 1-s, −100-pA injection revealing sag potentials in mPF. The dash line shows that sag is also evoked in mPF neurons with a 250-ms, −50-pA injection.
See related Figure S3 and Tables S4.1–S4.5.

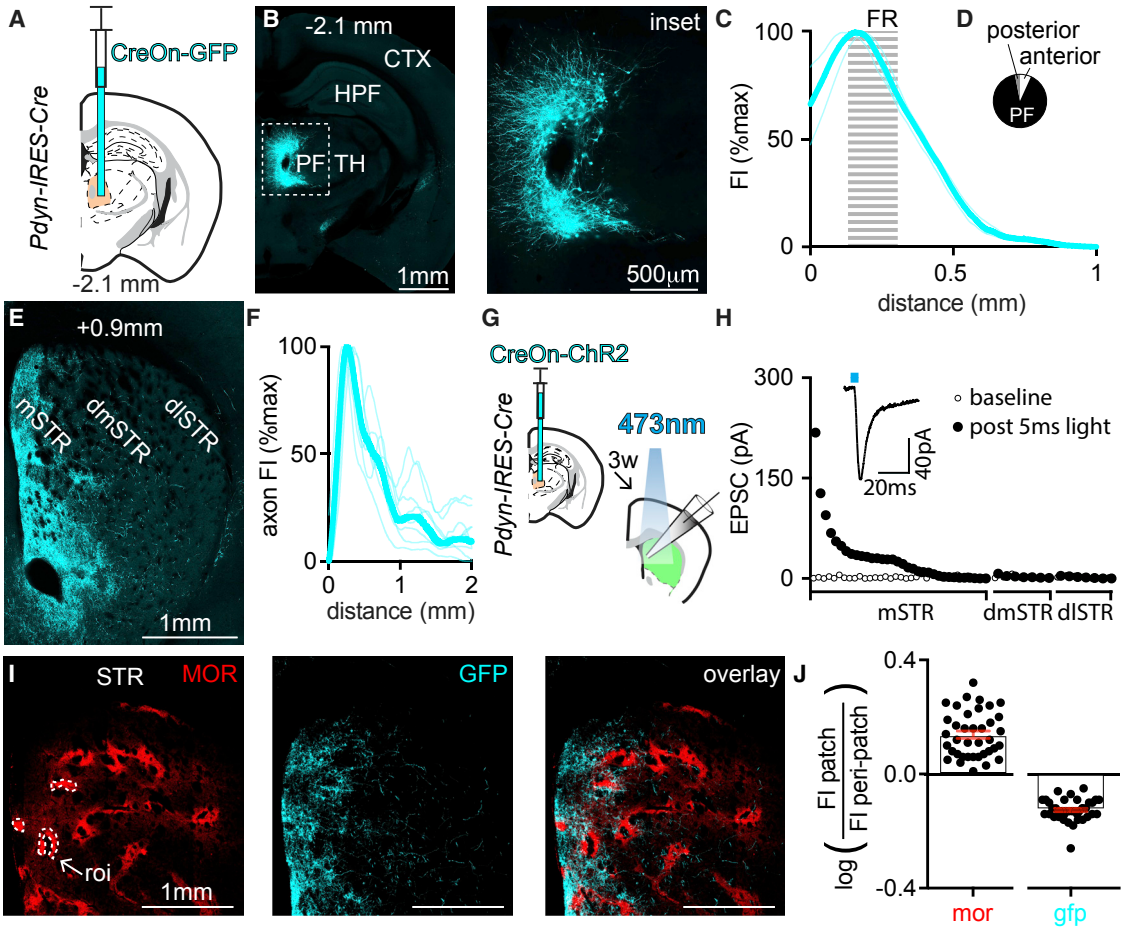

Figure 4. *Prodynorphin*-Expressing Cells Are Located in mPF and Target STR Matrix

(A) Schematic of a coronal section at −2.1 mm from a *Pdyn-IRES-Cre* mouse depicting an injection of CreOn-GFP (cyan) AAV into the PF.

(B) (Left) Coronal section at −2.1 mm showing that expression of GFP (cyan) is restricted to PF. The inset is enlarged (right) and shows medially projecting processes from the GFP-expressing neurons.

(C) Quantification of FI intensity in PF at coronal section −2.1 mm from images such as in (B). Thin lines show data from individual mice and the thick lines the mean (n = 3 mice). The dashed gray line represents the FR.

(D) Fraction of GFP+ cells anterior (An) or posterior (Po) to PF and in PF for the experiment shown in (A) (n = 1,670/2 cells/mice).

(E) Image of a coronal section highlighting the STR at +0.9 mm from a mouse manipulated as in (A). Dorsal STR is separated into sub-regions: expression of GFP-expressing *Pdyn*+ axons (cyan) from PF is seen in medial (mSTR), but not dorsal-medial (dmSTR) and dorsal-lateral (dlSTR), STR.

(F) Quantification of FI in STR of axons from *Pdyn*+ PF cells at coronal sections between +0.6 mm and +1.2 mm. Thin lines show data from individual mice and the thick line the mean (n = 9/3 slices/mice).

(G) Schematic of a coronal section at −2.1 mm (left), depicting injection of AAV encoding Cre-dependent channelrhodopsin (CreOn-Chr2) into PF of a *Pdyn-IRES-Cre* mouse. 3 weeks after virus injection, whole-cell recordings were obtained in STR (green) at and around coronal section +0.9 mm.

(H) EPSC amplitudes evoked by optogenetic stimulation of *Pdyn*+ PF terminals and measured in mSTR, dmSTR, and dlSTR SPNs. For each cell, the baseline current (open circle) and EPSC amplitude following a 5-ms light pulse (closed circle) are plotted (n = 48/4 cells/mice). Within each striatal region, EPSC amplitude is shown ranked from largest to smallest. Inset shows the mean of 10 light-evoked (blue line) EPSCs from one cell.

(I) Image of a coronal section of the STR at +0.9 mm with mu opioid receptors (MOR) immunolabeled (red, left) with 3 patches highlighted (white dashed lines). Axons of *Pdyn*+ PF neurons expressing GFP (center) avoid the MOR-rich patches (overlay, right).

(J) Quantification of the distribution of FI from GFP-labeled PF→mSTR axons in and around the MOR-rich patches. The log of the ratio of the mean MOR and GFP FI in the patch to that in a 100-µm-wide ring around the patch (peri-patch) is shown for 38 patches (n = 9/3 slices/mice).

See related Figure S4.

PF Neurons Are Not Locally Interconnected

The single-cell transcriptional data identified only excitatory neurons in PF; therefore, topographically organized PF→STR neurons are not interconnected by GABAergic interneurons. Several lines of analysis indicate that PF→STR neurons are also not interconnected by glutamatergic synapses. First, stimulation of ChR2 in *Pdyn-IRES-Cre* mPF neurons (Figure 5A) failed to elicit EPSCs in CTB-labeled, STR-projecting neurons in cPF (cPF→dmSTR = 0/19 EPSC; n = 3 mice) despite triggering suprathreshold currents in ChR2-expressing neurons in

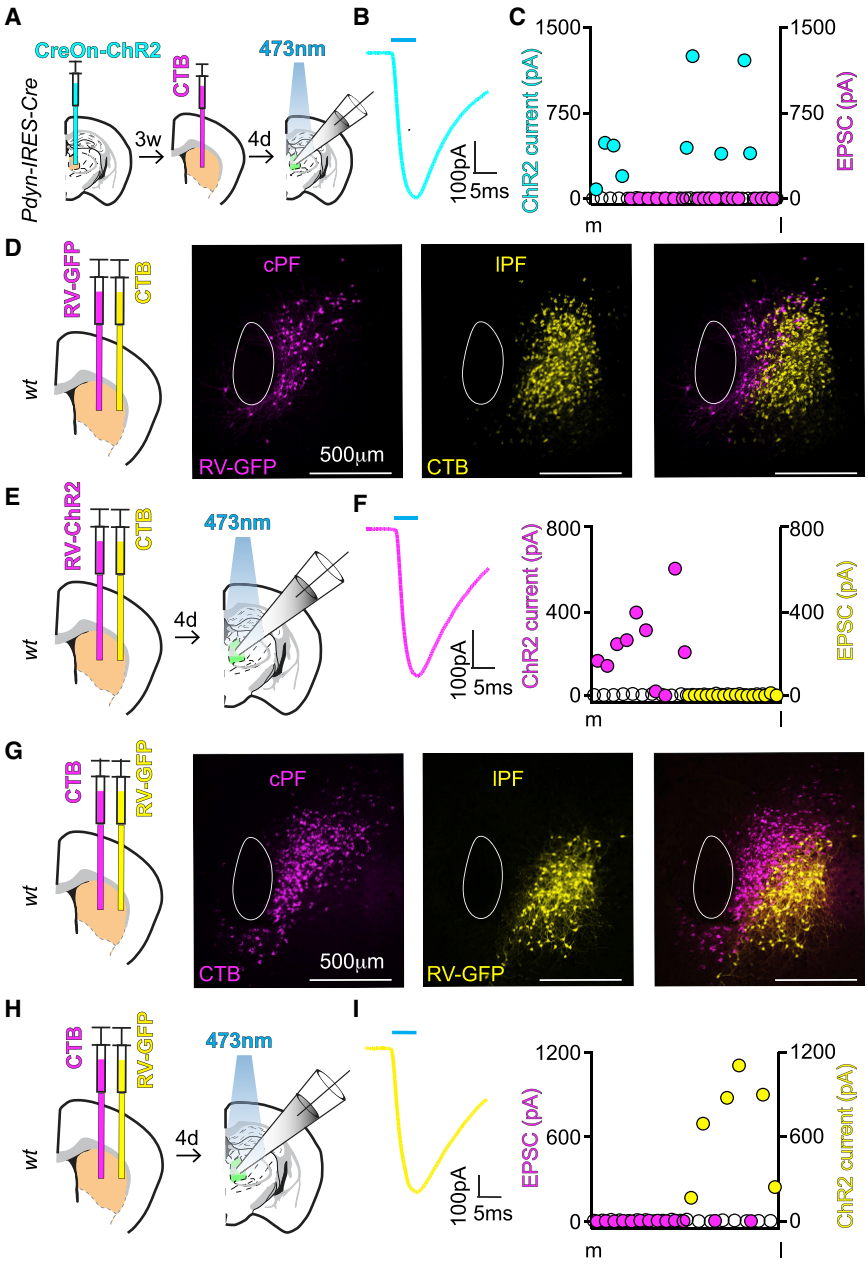

Figure 5. The Medial, Central, and Lateral Subcircuits of the PF Are Not Locally Interconnected

(A) (Left) Schematics of a coronal section at −2.1 mm depicting a viral injection of CreOn-ChR2 into the PF of a *Pdyn-IRES-Cre* mouse. (Center) Coronal section at +0.9 mm depicting CTB injection into dmSTR 3 weeks after the CreOn-ChR2 injection is shown. (Right) 4 days later, acute slices were cut and whole-cell recordings were obtained from ChR2+ or CTB+ cells.

(B) Example of light-evoked currents in ChR2+ mPF neurons, which are concurrent with the laser pulse.

(C) EPSC (CTB+ cells, magenta) and ChR2-current amplitudes (ChR2+ cells, cyan) in mPF and cPF evoked by optogenetic stimulation of *Pdyn-Cre*+ neurons. For each cell, the baseline (white circle) and light-evoked (colored circles) currents elicited by a 5-ms laser pulse (closed circle) are shown (n = 28/3 cells/mice). The circles are arranged according to the location of the cell along the medial to lateral direction. No EPSCs were detected in CTB+ cells.

(D) Experimental design showing a coronal section at +0.9 mm of a WT mouse depicting injection of RV-GFP and CTB into dmSTR and dlSTR, respectively. Images of resulting retrograde labeling in the PF (−2.1 mm) show expression of GFP (magenta) in cPF and CTB (yellow) in lPF. The overlay (right) shows largely not overlapped cell populations (n = 3 mice; example shown from one mouse).

(E) As (D) but with an injection of RV-ChR2 and followed by whole-cell recordings from ChR2+ or CTB+ cells 4 days after injections.

(F) (Left) As in (B), showing representative ChR2-mediated currents in ChR+ cPF neurons (magenta). (Right) Shown as in (C), with summary of amplitudes of light-evoked ChR2 currents (in magenta) and EPSCs in yellow. No EPSCs were detected in CTB+ cells (n = 26/2 cells/mice).

(G–I) As in (D)–(F) but with CTB injected into dmSTR and RV-GFP or RV-ChR2 into dlSTR (n = 19/2 cells/mice).

For (D) and (G), images are from 1 of 3 representative mice. See related Figure S5.

the same slices (549 pA ± 136 pA; 9/9 cells; Figures 5B and 5C). Second, non-pseudotyped rabies virus encoding GFP (RV-GFP) was used to fill cell bodies, axons, and dendrites of cPF → dmSTR neurons (Figure 5D); no overlap of these neurites with CTB-labeled, STR-projecting neurons in lPF was observed (Figure 5D). Similar experiments with RV-ChR2 injected into dmSTR and CTB into dlSTR (Figure 5E) resulted in light-induced currents large enough to induce APs in cPF neurons (237 pA ± 56 pA; 9/10 cells) but failed to evoke EPSCs in CTB+ cells in lPF → dlSTR neurons (lPF → dlSTR = 0/16 EPSC; n = 3 mice; Figure 5F). In addition, RV-mediated GFP and ChR2 expression in dlSTR-projecting lPF neurons did not overlap with neurites of dmSTR-projecting neurons in cPF (Figure 5G) and did not evoke EPSCs (cPF → dmSTR = 0/13 EPSC) despite suprathreshold ChR2 currents in lPF neurons (663 pA ± 155 pA; 6/6 cells; n = 2 mice; Figures 5H and 5I). Lastly, *trans*-synaptic RV labeling (Wickersham et al., 2007) revealed no connectivity across topographical zones of the PF from infected starter cells in mPF or lPF, despite clear labeling in other PF-projecting regions (substantia nigra reticulata [SNr] and superior colliculus [SC]; Figure S5).

Subclasses of PF Neurons Target Distinct Cortical Regions

Many thalamic nuclei project to and receive input from CTX (Sherman, 2016), forming circuits that modulate persistent

cortical activity (Guo et al., 2017). In primates, PF neurons innervate prefrontal CTX, whereas the histologically distinct CM neurons target motor and premotor areas (Parent and Parent, 2005). In rats, reconstructed PF cells project to STR and several cortical regions (Deschênes et al., 1996). However, studies of mouse PF, albeit using manipulations that could not specifically target this small nucleus, suggest that it does not project to CTX (Oh et al., 2014).

To determine whether mouse PF projects to CTX, CreOn-GFP was expressed in each PF subregion in separate mice. Automated image acquisition and analysis were used to measure and align the distribution of GFP-labeled axons in CTX (Figure 6A) across mice. STR-projecting neurons in each PF subregion in *Pdyn-IRES-Cre* mice were targeted by a specific viral strategy (Figures 6A and S6A; see STAR Methods). Furthermore, as expected for the PF→STR connectivity described above, GFP+ axons projected specifically between mPF→mSTR, cPF→dmSTR, and lPF→dlSTR (Figure 6B; Videos S3 and S4). The distribution of putative PF→CTX projections GFP+ axons was mapped to the ABA (Video S4), and the relative axon density (RAD) was measured as the fraction of all GFP+ pixels that are located in one area divided by the fraction of cortical volume contained in that area. This metric gives the relative enrichment of axons in each area compared to a uniform distribution of axons within CTX.

We focused on 2 coronal sections (from 0.6 to 1.2 mm and 2.5 to 3.1 mm anterior to posterior) and analyzed 11 cortical subregions (Figures 6C and 6H). The putative output of each PF cell class was not homogeneous in the posterior section (Figures 6D, 6E, and S6B; Table S2.2): for mPF, GFP-labeled axons were enriched in the limbic regions of CTX (RAD from mPF to: infralimbic area, ILA = 3.4 ± 0.7; anterior cingulate area ventral part, ACAv = 2.7 ± 0.8; agranular insular area dorsal part, AId = 3.9 ± 0.6; and argranular insular area ventral part, AIv = 1.9 ± 0.5; n = 3 mice; Figures 6D, 6E, and S6B) and less so in associative and somatosensory regions (secondary motor area, MOs = 0.9 ± 0.2; primary motor area, MOp = 0.3 ± 0.1; primary somatosensory cortex, SSp = 0.2 ± 0.0; n = 3 mice; Figures 6D, 6E, and S6B). cPF shares some of these medial and lateral limbic outputs with mPF but also projects to MOs and gustatory area (GU) (RAD from cPF to: MOs = 1.8 ± 0.3; GU = 3.3 ± 0.3; n = 4 mice; Figures 6D, 6E, and S6B). In contrast, lPF projects heavily to SSp, SSs, and also to the GU (RAD for lPF to: SSp = 1.5 ± 0.1; SSs = 4.4 ± 0.6; GU = 2.1 ± 0.4; n = 5 mice; Figures 6D, 6E, and S6B), with only few axons found elsewhere in CTX. To verify the differential projections from PF subregions, we injected CTB into posterior MOs or SSp: CTB+ cells were observed in cPF and lPF for the MOp and SSp injections, respectively (Figures 6F and 6G), thus confirming the results obtained with the measurements of RAD.

Similar analyses reveal that PF subregions also differentially target the more anterior section of cortex (Figures 6H–6J and S6B; Table S2.2). mPF projects strongly to the anterior cingulate area dorsal part (ACAd) and to the prelimbic area (PL) (RAD from mPF to: ACAd = 9.8 ± 2.6; PL = 4.4 ± 1.4; n = 3 mice; Figures 6I, 6J, and S6B), whereas cPF shares those targets but also projects to MOs (RAD from cPF to: ACAd = 6.2 ± 2.6; PL = 2.9 ± 1.6; MOs = 2.4 ± 0.6; n = 4 mice; Figures 6I, 6J, and S6B). This topography was generally maintained in the sections between these illustrative anterior and posterior regions (Figure S6C). Thus, STR-projecting PF neurons differentially innervate cortical regions: mPF and cPF innervate mainly limbic structures, whereas cPF also targets associative areas, such as MOs, and lPF selectively targets somatosensory cortical areas in the posterior CTX.

Cortical Layer 5 Projections to PF Are Topographically Organized and Form Feedforward Cortex-PF-Striatum Circuitry

Some thalamic nuclei modulate sequential processing stages in CTX by receiving input from an upstream region and projecting to its downstream target, thus adding a parallel processing stage linking regions in CTX that are also themselves interconnected (Sherman, 2016). For example, the pulvinar mediates a CTX-TH-CTX projection to facilitate transmission of information about attentional priorities between two visual cortical areas that are also directly connected (Saalmann et al., 2012). Because CTX is analogously upstream to the STR, we hypothesized that the CTX-TH-CTX circuit organization might be recapitulated in circuits between CTX, PF, and STR (Saalmann, 2014).

To examine whether the regions of CTX that receive input from specific subregions of PF (Figure 6) project back to those same regions of PF, we virally expressed GFP in layer 5 projection neurons, including those that project to STR (Gerfen et al., 2013) in *Tg(Rbp4-cre)KL100Gsat* mice (Gong et al., 2007; in short, *Rbp4-Cre*) and labeled PF→STR projection neurons by focal injection of CTB into STR (Figure 7). Layer 5 neurons were targeted because they give rise to the cortical outputs that participate in CTX-TH-CTX circuits described above (Sherman, 2016). Targeting MOs axons and cPF→dmSTR cell bodies in cPF (max FI of CTB in: cPF = 67 ± 8; in rest [r] of PF = 8% ± 1%; n = 14/3 slices/mice) revealed that MOs axons in PF preferentially overlap with CTB+ cell bodies in cPF (max axon FI overlap in: cPF = 86% ± 3%; rPF = 30% ± 5%; n = 14/3; slices/mice) across all coronal sections of PF (Figures 7A–7C and S7A). Similar analysis of SSp and lPF→dlSTR neurons (max FI of CTB in: lPF = 60% ± 13%; rPF = 6% ± 1%; n = 8/2; slices/mice) revealed overlap of SSp axons and CTB-labeled lPF neurons (log ratio of axon FI in the lPF/rPF = 0.47 ± 0.07; n = 8/2 slices/mice; Figures 7D–7F and S7B). Conversely, selective targeting of SSp and cPF revealed no overlap between the CTB+ cells and axons, confirming the specificity of SSp→lPF axon topography (log ratio of axon FI in the cPF/rPF = −0.76 ± 0.10; n = 11/2 slices/mice; Figure 7G).

Targeting PFC and mPF→mSTR (max FI of CTB in: mPF = 75% ± 7%; rPF = 18% ± 1%) revealed overlap of PFC axons and CTB-labeled mPF neurons (log ratio of axon FI mPF/rPF = 0.29 ± 0.03; n = 12/2 slices/mice; Figures 7H–7J and S7C). In contrast, PFC axons overlapped little with cPF→dmSTR neurons (log ratio of axon FI in the cPF/rPF = 0.02 ± 0.04; Figure 7K). Lastly, axons from PFC also overlapped with mPF→mSTR neurons CONTRA to the injection site in CTX (max FI of CTB: CONTRA-mPF = 64% ± 9%; CONTRA-rPF = 12% ± 2%; for max axon FI overlap in: CONTRA-mPF = 67% ± 9%; CONTRA-rPF = 27% ± 2%; n = 10/2 slices/mice; Figures 7L–7N and S7D) compared to MOs and SSp, which sparsely projected to CONTRA-PF in comparison to PF IPSI to the injection

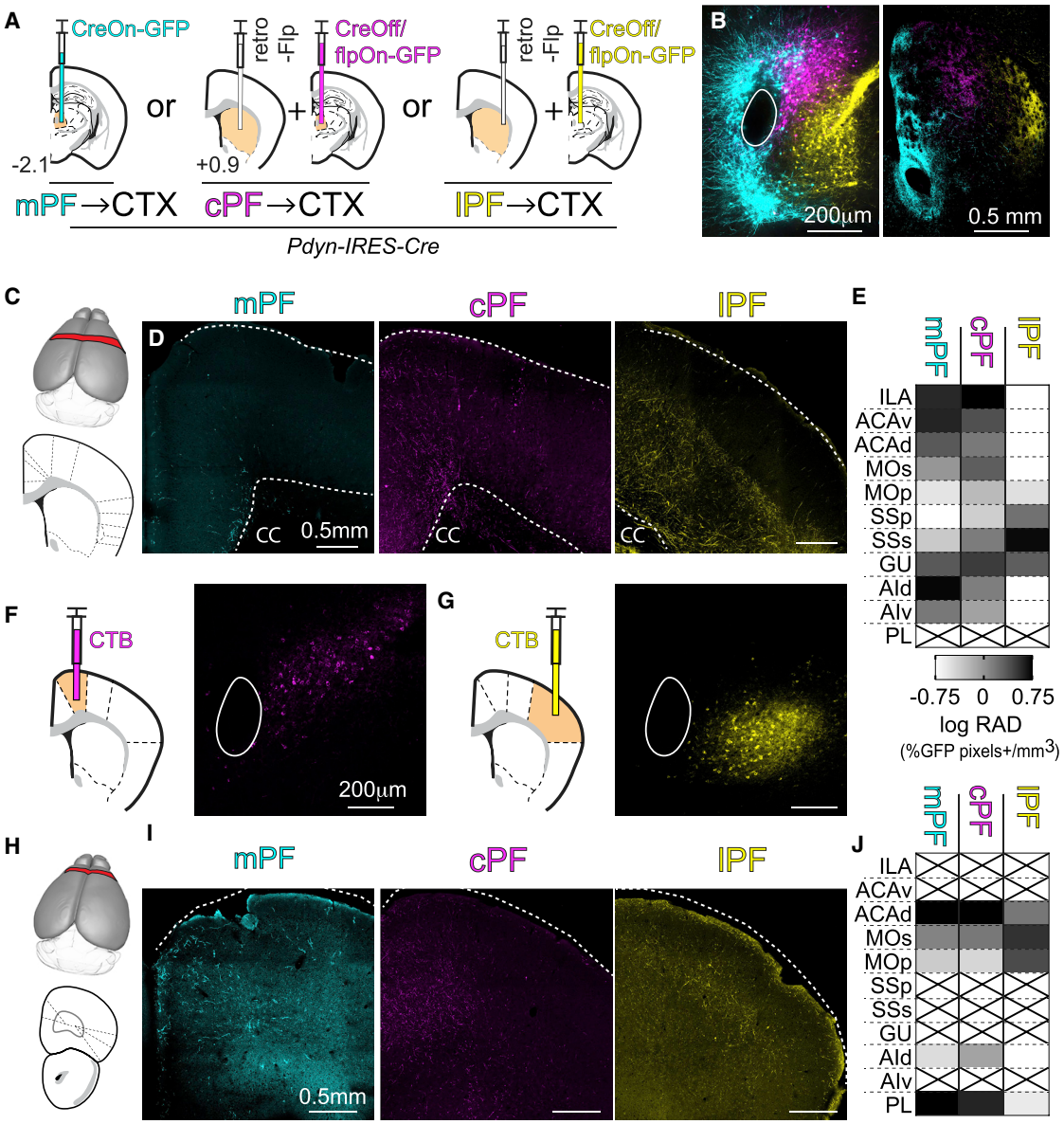

Figure 6. PF→Striatum Neurons Send Topographically Organized Projection to CTX

(A) Schematics of the intersectional strategies in *Pdyn-IRES-Cre* mice used to express GFP in subsets of PF→STR neurons. (Left) Injection of CreOn-GFP (cyan) into PF results in expression of GFP in the medial *Pdyn*+ neurons. Injection of retro-Flp (black) in dmSTR (center) or dlSTR (right) and CreOff-FlpOn-GFP (magenta) into PF achieves expression in cPF or lPF, respectively, while avoiding it in *Pdyn*+ neurons.

(B) Overlay of 1 brain section of each of 3 brains targeted with the labeling strategies depicted in (A) at coronal section −2.1 mm in PF (left) and at +0.9 mm in STR (right).

(C) (Top) For the analysis of the distribution of GFP+ axons in CTX, a region spanning from 0.6 to 1.2 mm anterior posterior was taken (red). (Bottom) Regions of interest were chosen, spanning the medial lateral portion of CTX as demarcated by dashed lines.

(D) Representative coronal sections from the posterior region of CTX (0.9 mm) for each of the labeling strategies (left: mPF→CTX; center: cPF→CTX; right: lPF→CTX), highlighting the differential projections to medial, central, and lateral parts of CTX, respectively. CC, corpus callosum.

(E) Example quantification of the relative axon density (RAD) of PF axons arising from each subregion measured in each of 11 cortical regions. The log(RAD) per region is represented by the gray scale spanning ±0.75 log units. An X indicates a cortical region not present in the analyzed slice.

(F) Experimental design showing a coronal section at 0.9 mm depicting an injection of CTB into MOs (left) and the resulting labeling in cPF at the −2.1 mm coronal section (right).

(G) As in (F) but targeting SSp with CTB (left), resulting in labeling in lPF (right).

(H–J) As in (C)–(E) but showing the analysis in an anterior section in CTX spanning 2.5–3.1 mm.

The images shown in (B), (D), and (I) are from the same 3 mice. See related Figure S6, Videos S3 and S4, and Table S2.2.

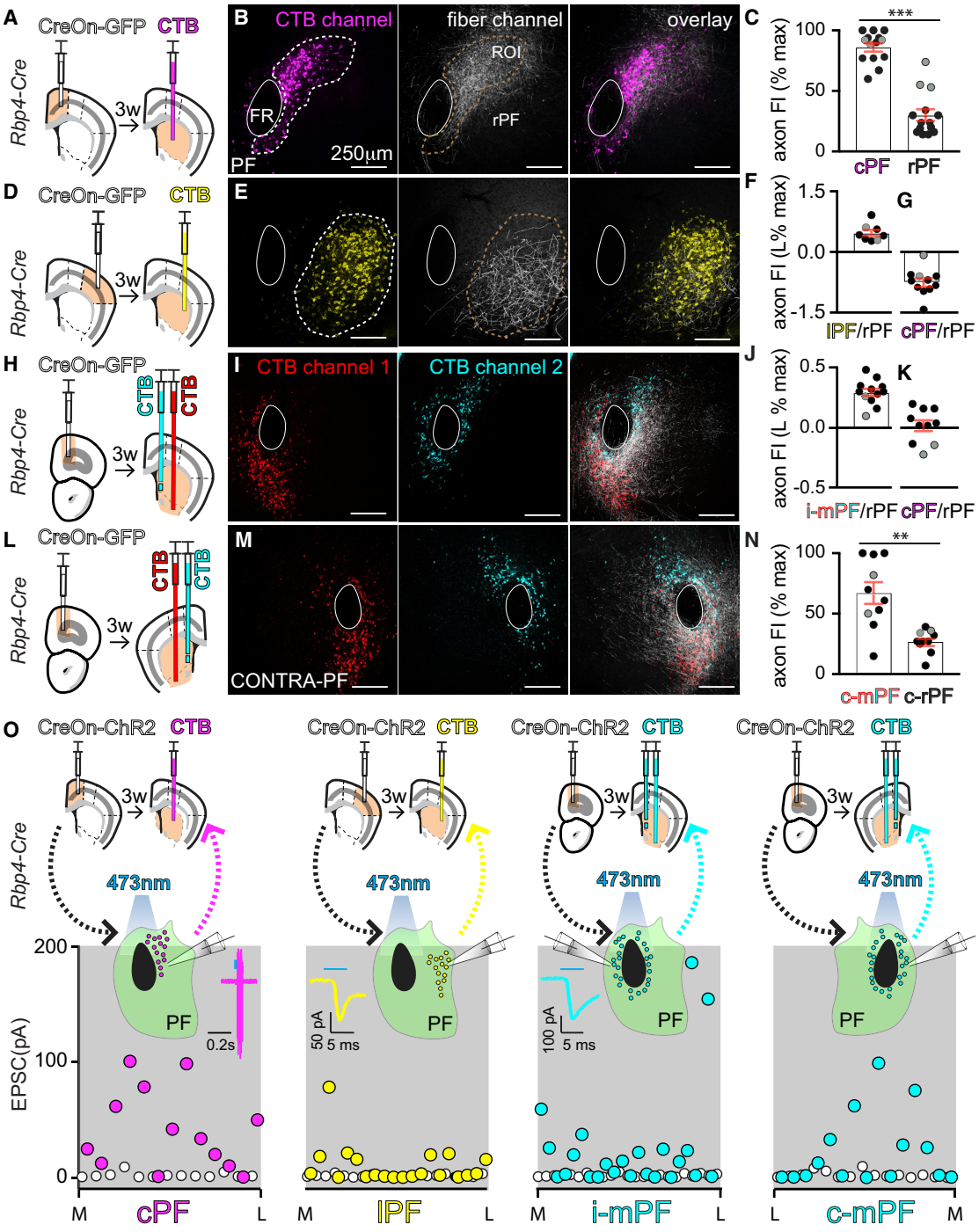

Figure 7. Cortical Layer 5 Projections to PF Are Topographically Organized and Form Closed CTX-PF-STR Circuits

(A) Schematic of coronal sections at +0.9 mm from an *Rbp4-Cre* mouse depicting injection of CreOn-GFP (white) into layer 5 of secondary motor CTX (MOs) followed by CTB (magenta) into dmSTR 3 weeks later.

(B) Coronal section at −2.1 mm in PF showing the results of the experiment in (A). CTB (magenta) and GFP-expressing axons from MOs (white) are seen to overlap in cPF. The region of interest (ROI) in the CTB channel (white dashed line) was manually drawn and applied to the GFP channel to measure the FI distribution.

(C) Quantification of % of the maximal GFP FI in the cPF ROI, as shown in (B), compared to that in the rest of PF (rPF). Grey filled circles here (and throughout the figure) show data from coronal section −2.3 mm in PF (n = 14/3 slices/mice; p = 0.0001; Wilcoxon test).

(D and E) As in (A) and (B) but with injection of CreOn-GFP into primary sensory CTX (SSp; white) and CTB (yellow) into dlSTR.

(F) (Left) Quantification of % of the maximal FI of GFP-labeled axons in the lPF ROI, as shown in (E), compared to that in the rest of PF (rPF) on a log scale (n = 8/2 slices/mice).

(legend continued on next page)

site (max axon FI: MOs→IPSI-PF = 89% ± 2% versus MOs→CONTRA-PF = 7% ± 0.5%; n = 14/2 slices/mice; SSp→IPSI-PF = 77% ± 6% versus SSp→CONTRA-PF = 2% ± 0.3%; n = 11/2 slices/mice; and PFC→IPSI-PF = 75% ± 6% versus PFC→CONTRA-PF = 30% ± 3%; n = 11/2 slices/mice; Figures S8A–S8E).

To determine whether regions of CTX and PF that project to the same region of STR are themselves connected, we expressed ChR2 in *Rbp4-Cre* neurons in regions of CTX and labeled PF→STR neurons by CTB injection in STR. We relied on comprehensive maps of CTX→STR projections (Hunnicutt et al., 2016; Hintiryan et al., 2016; Hooks et al., 2018) and our own analysis of the topography of PF→STR (Figure 2) and PF→CTX projections (Figure 6) to select regions of STR for CTB injection. Whole-cell voltage-clamp recordings from CTB+ cells in PF revealed optogenetically triggered EPSCs in PF→STR neurons for all the CTX→PF projections tested (MOs→cPF = 11/13 EPSCs, n = 2 mice; SSp→lPF = 7/21, n = 2 mice; PFC→IPSI-mPF = 12/23, n = 3 mice; PFC→CONTRA-mPF = 7/15, n = 2 mice; Figure 7O). In addition, the inputs were specific to the target region and did not evoke EPSCs in neighboring subregions (Figures S8F and S8G). Thus, we find selective innervation of anatomically defined PF subregions by specific cortical regions.

In summary, projections from PF to STR and CTX are organized into parallel CTX-PF-CTX and CTX-PF-STR motifs: subregions of PF and CTX are reciprocally connected and these linked subregions each target the same STR domain.

Differential Modulation of STR Neurons by Each PF Neuron Subclass

Previous work compared PF→STR projections to those from other thalamic nuclei (Ellender et al., 2013; Alloway et al., 2014). We find that PF has multiple neuron classes that target distinct regions of STR and CTX and receive disparate inputs from CTX and the midbrain. Each channel may also have distinct effects on STR by differentially targeting STR neurons. To determine whether the PF subclasses differently innervate interneurons in STR, whole-cell recordings were made from either cPF→dmSTR or lPF→dlSTR projections in *Tg(Lhx6-EGFP)BP221Gsat* BAC transgenic mice (Gong et al., 2007; in short, *Lhx6-EGFP*), which express GFP in low-threshold spiking interneurons (LTSIs) and fast spiking interneurons (FSIs), but not SPNs (Gittis et al., 2010; Figures 8A and 8C). PF to SPNs connectivity was similarly high for both cPF→dmSTR (14/20 SPNs; n = 5 mice) and lPF→dlSTR (17/25; n = 7 mice) neurons (Figures 8B and 8D). However, in the same mice, PF connectivity to FSIs, identified based on passive and active properties (Saunders et al., 2016), was low between cPF→dmSTR (2/23 FSIs innervated) compared to lPF→dlSTR (9/14 FSIs; Figures 8B and 8D). Inputs to LTSIs, also identified based on electrophysiological properties, was low from both cPF (0/11 LTSIs innervated) and lPF (3/26 LTSIs; Figures 8B and 8D). In a separate experiment, whole-cell recordings in WT mice revealed innervation of tonically active interneurons (TANs) by cPF→dmSTR (7/10 TANs innervated) and lPF→dlSTR (4/10 TANs) neurons (Figures 8B and 8D). LTSIs and FSIs innervation by mPF→mSTR neurons was not examined; however, mPF to SPN (24/33 SPNs; n = 4 mice; Figure 4H) and to TAN (7/9 TANs innervated; n = 2 mice) connectivity was similar to that of cPF→dmSTR and lPF→dlSTR projections. Thus, we find that topographically defined PF→STR projections robustly target SPNs and TANs but differently innervate STR LTSIs and FSIs.

The NMDA receptor (NMDAR) component of the SPNs glutamatergic EPSCs mediates induction of plateau potentials (up states) in SPNs (Plotkin et al., 2011). Previous studies report widely varying NMDA- (NMDAR) to AMPA-type (AMPAR) glutamate receptor current ratios at PF to SPN synapses: analyses in mice describe that CTX→STR synapses induce high NMDAR/AMPAR current ratios compared to TH→STR synapses (Ding et al., 2008), whereas the opposite result has been described in rats (Smeal et al., 2007). We reasoned that these differences might actually arise from differences in the PF→STR projections studied. Therefore, we measured AMPAR- and NMDAR-mediated synaptic currents for the 3 subclasses of PF→STR projections (Figure 8E). NMDAR/AMPAR currents ratio was higher at mPF→mSTR synapses (3.8 ± 0.2; n = 17/2 cells/mice) compared to cPF→dmSTR (1.6 ± 0.1; n = 43/4 cells/mice) and lPF→dlSTR (1.9 ± 0.2; n = 19/3 cells/mice; Figures 8E–8G). Thus, the characteristics of PF→SPN excitatory synapses depend on the target region within the STR.

DISCUSSION

Here, we present a comprehensive cellular and circuit analysis of the PF, a major sub-cortical excitatory input to the STR. Based on its anatomical, transcriptional, electrophysiological, and synaptic properties, we place PF projection neurons into 3 classes. mPF neurons expressed *Pdyn*, the precursor protein for the K-opioid receptor agonist dynorphin, project to matrix

(G) As in (F) but following injection of CreOn-GFP into primary SSp and CTB into dmSTR and not dlSTR, resulting in CTB in the cPF→dmSTR projections. This confirmed the specificity of SSp→lPF projection topography (n = 11/2 slices/mice).
(H–J) As in (D)–(F) but for injection of CreOn-GFP into PFC (white) and CTB into mSTR (cyan) and ACB (red) (n = 12/2 slices/mice).
(K) As in (G) but with an injection of CreOn-GFP into PFC and CTB into dmSTR. This confirmed the specificity of PFC→mPF axon topography (n = 10/2 slices/mice).
(L–N) As in (A)–(C) but for injection of CreOn-GFP into PFC and CTB into mSTR and ACB CONTRA to the injection in PFC (n = 10/2 slices/mice; p = 0.002; Wilcoxon test).
(O) (Top) Schematics of 4 experimental paradigms using *Rbp4-Cre* mice, indicating the sites of injection of CreOn-ChR2 into CTX and CTB into STR 3 weeks later. Acute slices were cut (bottom), and ChR2-evoked corticothalamic EPSCs were measured in CTB+ neurons in cPF (n = 13/2; cells/mice), lPF (n = 13/2), mPF IPSI (i-mPF n = 23/3), and CONTRA (c-mPF n = 15/2) to the cortical injection. The amplitudes of the ESPC (open circles) and equivalent analysis during a baseline period (closed circles) are shown as in previous figures. Overlay of 10 APs from a cell in cPF (magenta) highlighting that the CTX→PF terminals are sufficient to spike PF neurons. Example EPSCs are shown for lPF (yellow) and mPF (cyan) cells.
Grey filled circles in (C), (F), (G), (J), (K), and (N) represent the analyses of coronal section −2.3 mm in PF. See related Figures S7 and S8.

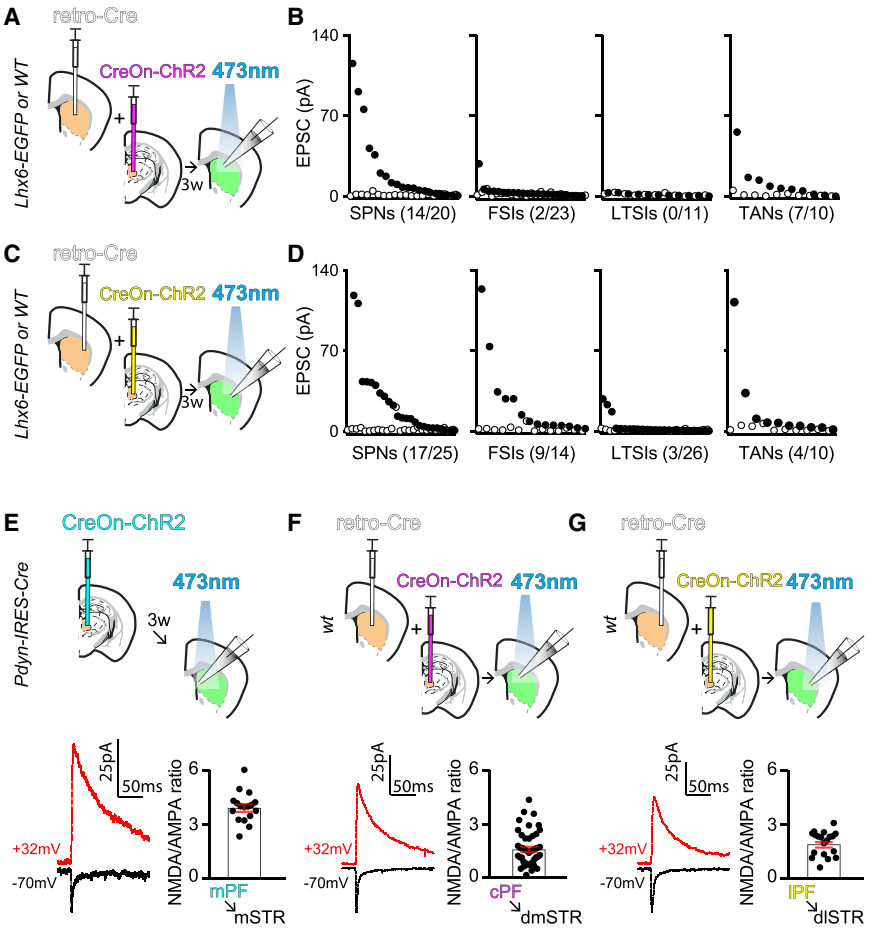

Figure 8. Differential Modulation of STR Neurons by PF Subclasses

(A) Schematic of coronal sections at +0.9 mm from a *Lhx6-EGFP* or WT mouse injected with retro-Cre (white) in dmSTR and CreOn-ChR2 (magenta) in PF. 3 weeks later, acute slices were cut and ChR2-evoked cPF→dmSTR EPSCs were measured.

(B) Amplitudes of EPSC from (left to right) SPNs, FSI, LTSI, and TANs in dmSTR. The amplitudes of the ESPC (open circles) and noise during a baseline period (closed circles) are shown (n = 5 mice).

(C and D) As in (A) and (B) but with injections of retro-Cre (white) in dlSTR and CreOn-ChR2 (yellow) in PF (n = 7 mice).

(E) (Top) Schematic of coronal sections at −2.1 mm from a *Pdyn-IRES-Cre* mouse injected with CreOn-Chr2 in PF. 3 weeks later, whole-cell recordings were obtained in STR (highlighted in green). Light-evoked EPSCs were recorded at −70 mV and at a holding potential 20 mV above the EPSC the reversal potential in each cell. (Bottom left) Representative traces of NMDA (red)- and AMPA (black)-receptor-mediated EPSCs are shown. (Bottom right) Summary data are shown (n = 17/2 cells/mice).

(F and G) As in (E) but for injection of retro-Cre in dmSTR (F) or dlSTR (G) followed by injection of CreOn-ChR2 into PF. For (F), n = 43/4 and, for (G), n = 19/3 cells/mice.

compartments of mSTR and to limbic CTX (e.g., agranular insular, infra-, and pre-limbic CTX), and receive bilateral input from layer 5 in PFC. mPF→STR projection neurons have higher input resistance, lower capacitance, and higher resting potential relative to those in central and lateral aspects of the PF. In addition, these neurons have prominent sag potentials, a feature predicted from the single-cell transcriptional analysis showing expression of the *Hcn1* gene. In cPF, neurons express *Tnc*, project to dmSTR and to limbic and associative regions of CTX (e.g., to infralimbic, secondary motor, and gustatory CTX), and receive input from layer 5 of associative areas (secondary motor). Lastly, in lPF, neurons express *Spon1*, project to dlSTR and predominantly somatosensory regions of CTX (e.g., primary and secondary somatosensory CTX), and receive input from layer 5 of SSp. All cell classes in PF have high connectivity to SPNs but differ in their innervation of STR interneurons. Neurons do not interconnect across regions in PF, suggesting that PF subregions do not intermix their incoming cortical and midbrain signals through local inhibitory or excitatory connectivity.

Comparison of Mouse PF to that of Other Species

The anatomical organization that we describe for mouse PF→STR is present in other species (Giménez-Amaya et al., 2000; Jones, 2007). Primate PF/CM is also subdivided into 3 regions that preferentially innervate motor CTX (lateral CM), sensory motor STR (medial CM), and associative limbic STR (PF; Sadikot and Rymar, 2009). In primates, CM and PF are also distinguished based on cell density and size (Jones, 2007), vulnerability to disease (Henderson et al., 2000), as well as *in vivo* firing patterns (Matsumoto et al., 2001) and have been proposed to have different functions (Glimcher and Lau, 2005; Smith et al., 2014). In rats, lPF projects to dlSTR and mPF projects to dmSTR (Berendse and Groenewegen, 1990), which is a similar, albeit a simplified version of the relationship observed between CM, PF, and STR in primates. Nevertheless, no region in the rat TH has been defined as CM due to the lack of a clear histological boundary.

It is widely accepted that the gross nuclear division of the mouse TH is similar to that in rats (Jones, 2007), although some thalamic nuclear boundaries are more obscure in mice, likely due to a diffuse cytoarchitecture. The facility of analysis in mice allowed us to uncover differences between subdivisions of the PF that have not been addressable in traditionally genetically intractable species, such as primates, cats, and rats. Even within mouse studies, PF has been treated as being cellularly homogeneous, not having subcircuits, and not being distinct from neighboring TH nuclei (Parker et al., 2016; Kato et al., 2011; Aceves Buendia et al., 2017; Assous et al., 2017; Choi et al., 2018). Our findings reveal transcriptional distinctions that delineate PF neuron classes and separate PF from the medial dorsal nucleus in the anterior-posterior axis and the posterior nucleus in medial-lateral axis. Thus, these results permit targeted analyses of specific PF subcircuits and neuron classes in normal

behavior and disease models, similar to studies already underway in other brain regions (Wallace et al., 2017).

PF-CTX Interactions

Thalamic nuclei typically form reciprocal connections with CTX by receiving input from and projecting to a single cortical region or receiving input from one region and project to another (Sherman, 2016). Thalamic nuclei receive modulatory inputs from layer 6, whereas higher-order thalamic nuclei also receive inputs from layer 5 (Harris and Shepherd, 2015; Sherman, 2016; Jeong et al., 2016). These CTX-TH-CTX circuits have been proposed to have two functions. First, via recurrent excitation, they maintain persistent activity in CTX, as has been shown for projections from motor TH to the anterior lateral motor region of CTX (Guo et al., 2017), which is thought to be necessary for working memory (Bolkan et al., 2017; Halassa and Kastner, 2017). Second, other CTX-TH-CTX circuits have a triangular motif, in which a cortical region targets a second cortical area and a thalamic nucleus that also projects to the second cortical region. This motif, for example, is seen in Pulvinar outputs to visual cortices and has been proposed to transmit and synchronize signals about attentional priorities between directly connected cortical regions (Saalmann et al., 2012). These canonical principals of organization have not been examined fully for ILM TH and its interactions with CTX.

PF→CTX projections align with CTX→PF projections, suggesting a corticothalamic recurrent network through PF. However, unlike typical TH nuclei, the main output of PF is to STR and not to CTX. For this reason, and analogous to the triangle attentional motif described above, we propose that CTX-PF-CTX circuits facilitate and shape the striatal output of the associated cortical region. PF can integrate information from CTX with that from sub-cortical nuclei (such as SC and SNr) to facilitate correct action selection in an ongoing sensorimotor context. Because we find that PF neuron classes are not interconnected in PF, these networks of activity can act relatively independently of each other, although other potentially diffuse external inputs, such as from the thalamic reticular nucleus, may coordinate activity across PF subregions.

We find that PFC projects bilaterally to mPF, whereas SSP→lPF or MOs→cPF projections are strictly IPSI, highlighting the potential different functions of the PF subclasses characterized here—laterality may be important to maintain sensory and associative circuits although perhaps a global limbic signal may need to be dispersed across both hemispheres. PT cortical neurons do not project to contralateral STR (Harris and Shepherd, 2015); thus, the bilateral PFC→mPF projections may transmit PT-related activity signal near synchronously to both STR via PF without recruitment of the bilateral intratelencephalic (IT)-type cortical projections.

STAR★METHODS

Detailed methods are provided in the online version of this paper and include the following:

- KEY RESOURCES TABLE
- CONTACT FOR REAGENT AND RESOURCE SHARING
- EXPERIMENTAL MODEL AND SUBJECT DETAILS
  - Mice
- METHOD DETAILS
  - AAVs
  - Rabies viruses
  - Stereotaxic Intracranial Injections
  - Injection coordinates
  - Injection volumes and waiting time for specific anatomical regions and reagents
  - Histology and Imaging for STPT
  - Histology and imaging for all other experiments
  - Immunohistochemistry
  - *In situ* hybridization
  - Whole-cell dissociation and RNA capture
  - Acute Brain Slice Preparation and Whole-Cell Recordings
  - PF subregion targeting strategies used in Figure 6
- QUANTIFICATION AND STATISTICAL ANALYSIS
  - General
  - STPT cell count Image Analysis
  - Brain volume quantification
  - Projection mapping data processing
  - Image analysis for all other experiments
  - InDrops Analysis
  - Electrophysiological Analysis
- DATA AND SOFTWARE AVAILABILITY

SUPPLEMENTAL INFORMATION

Supplemental Information can be found with this article online at https://doi.org/10.1016/j.neuron.2019.02.035.

ACKNOWLEDGMENTS

We thank members of the Sabatini lab, Dr. Assad, Dr. Harvey, Dr. Cox, Dr. Hart, and Dr. Ruiz for helpful discussions. We thank J. Levasseur for mouse husbandry and genotyping, J. Saulnier and L. Worth for lab administration, and Dr. L. Ding and D. Tom at the Enhanced Neuroimaging Core of the Harvard NeuroDiscovery Center for FIJI image analysis macros. We thank S. Knemeyer (http://sigrid.knemeyer.com/) for assistance with graphical design. Starting materials for generating rabies viruses were a generous gift from Dr. B.K. Lim (UCSD). This work was supported by grants from NIH (R01NS103226 B.L.S./P.O.; P30NS072030, Neurobiology Imaging Center), the Simons Collaboration on the Global Brain (543037SPI, B.L.S.), and Harvard Society of Junior Fellows (D.R.H.).

AUTHOR CONTRIBUTIONS

Conceptualization, G.M. and B.L.S.; Methodology, G.M., J.T., T.M.H., D.R.H., K.W.H., M.H., C.S., W.W., P.O., and B.L.S.; Software, G.M., J.T., T.M.H., D.R.H., K.U.V., and B.L.S.; Formal Analysis, G.M., J.T., D.R.H., K.U.V., and B.L.S.; Investigation, G.M., J.T., T.M.H., D.R.H., K.W.H., M.H., C.S., W.W., and K.R.; Writing – Original Draft, G.M. and B.L.S.; Writing – Review & Editing, all authors; Visualization, G.M., J.T., D.R.H., and B.L.S.; Supervision, P.O. and B.L.S.

DECLARATION OF INTERESTS

The authors declare no competing interests.

Received: July 2, 2018
Revised: January 3, 2019
Accepted: February 20, 2019
Published: March 21, 2019

REFERENCES

Aceves Buendia, J.J., Tiroshi, L., Chiu, W.H., and Goldberg, J.A. (2017). Selective remodeling of glutamatergic transmission to striatal cholinergic interneurons after dopamine depletion. Eur. J. Neurosci. *18*, 63.

Alloway, K.D., Smith, J.B., and Watson, G.D.R. (2014). Thalamostriatal projections from the medial posterior and parafascicular nuclei have distinct topographic and physiologic properties. J. Neurophysiol. *111*, 36–50.

Assous, M., Kaminer, J., Shah, F., Garg, A., Koós, T., and Tepper, J.M. (2017). Differential processing of thalamic information via distinct striatal interneuron circuits. Nat. Commun. *8*, 15860.

Berendse, H.W., and Groenewegen, H.J. (1990). Organization of the thalamostriatal projections in the rat, with special emphasis on the ventral striatum. J. Comp. Neurol. *299*, 187–228.

Bezgin, G., Reid, A.T., Schubert, D., and Kötter, R. (2009). Matching spatial with ontological brain regions using Java tools for visualization, database access, and integrated data analysis. Neuroinformatics *7*, 7–22.

Bolkan, S.S., Stujenske, J.M., Parnaudeau, S., Spellman, T.J., Rauffenbart, C., Abbas, A.I., Harris, A.Z., Gordon, J.A., and Kellendonk, C. (2017). Thalamic projections sustain prefrontal activity during working memory maintenance. Nat. Neurosci. *20*, 987–996.

Bradfield, L.A., Hart, G., and Balleine, B.W. (2013). The role of the anterior, mediodorsal, and parafascicular thalamus in instrumental conditioning. Front. Syst. Neurosci. *7*, 51.

Choi, K., Holly, E.N., Davatolhagh, M.F., Beier, K.T., and Fuccillo, M.V. (2018). Integrated anatomical and physiological mapping of striatal afferent projections. Eur. J. Neurosci. *8*, 15860.

Chung, K., Wallace, J., Kim, S.-Y., Kalyanasundaram, S., Andalman, A.S., Davidson, T.J., Mirzabekov, J.J., Zalocusky, K.A., Mattis, J., Denisin, A.K., et al. (2013). Structural and molecular interrogation of intact biological systems. Nature *497*, 332–337.

Conte, W.L., Kamishina, H., and Reep, R.L. (2009). Multiple neuroanatomical tract-tracing using fluorescent Alexa Fluor conjugates of cholera toxin subunit B in rats. Nat. Protoc. *4*, 1157–1166.

Cowan, W.M., and Powell, T.P. (1956). A study of thalamo-striate relations in the monkey. Brain *79*, 364–390.

DeLong, M.R. (1990). Primate models of movement disorders of basal ganglia origin. Trends Neurosci. *13*, 281–285.

Deschênes, M., Bourassa, J., Doan, V.D., and Parent, A. (1996). A single-cell study of the axonal projections arising from the posterior intralaminar thalamic nuclei in the rat. Eur. J. Neurosci. *8*, 329–343.

Ding, J., Peterson, J.D., and Surmeier, D.J. (2008). Corticostriatal and thalamostriatal synapses have distinctive properties. J. Neurosci. *28*, 6483–6492.

Ellender, T.J., Harwood, J., Kosillo, P., Capogna, M., and Bolam, J.P. (2013). Heterogeneous properties of central lateral and parafascicular thalamic synapses in the striatum. J. Physiol. *591*, 257–272.

Gerfen, C.R., Paletzki, R., and Heintz, N. (2013). GENSAT BAC cre-recombinase driver lines to study the functional organization of cerebral cortical and basal ganglia circuits. Neuron *80*, 1368–1383.

Giménez-Amaya, J.M., de las Heras, S., Erro, E., Mengual, E., and Lanciego, J.L. (2000). Considerations on the thalamostriatal system with some functional implications. Histol. Histopathol. *15*, 1285–1292.

Gittis, A.H., Nelson, A.B., Thwin, M.T., Palop, J.J., and Kreitzer, A.C. (2010). Distinct roles of GABAergic interneurons in the regulation of striatal output pathways. J. Neurosci. *30*, 2223–2234.

Glimcher, P.W., and Lau, B. (2005). Rethinking the thalamus. Nat. Neurosci. *8*, 983–984.

Gong, S., Doughty, M., Harbaugh, C.R., Cummins, A., Hatten, M.E., Heintz, N., and Gerfen, C.R. (2007). Targeting Cre recombinase to specific neuron populations with bacterial artificial chromosome constructs. J. Neurosci. *27*, 9817–9823.

Guo, Z.V., Inagaki, H.K., Daie, K., Druckmann, S., Gerfen, C.R., and Svoboda, K. (2017). Maintenance of persistent activity in a frontal thalamocortical loop. Nature *545*, 181–186.

Halassa, M.M., and Kastner, S. (2017). Thalamic functions in distributed cognitive control. Nat. Neurosci. *20*, 1669–1679.

Harris, K.D., and Shepherd, G.M.G. (2015). The neocortical circuit: themes and variations. Nat. Neurosci. *18*, 170–181.

Henderson, J.M., Carpenter, K., Cartwright, H., and Halliday, G.M. (2000). Degeneration of the centré median-parafascicular complex in Parkinson's disease. Ann. Neurol. *47*, 345–352.

Herkenham, M., and Pert, C.B. (1981). Mosaic distribution of opiate receptors, parafascicular projections and acetylcholinesterase in rat striatum. Nature *291*, 415–418.

Hintiryan, H., Foster, N.N., Bowman, I., Bay, M., Song, M.Y., Gou, L., Yamashita, S., Bienkowski, M.S., Zingg, B., Zhu, M., et al. (2016). The mouse cortico-striatal projectome. Nat. Neurosci. *19*, 1100–1114.

Hooks, B.M., Papale, A.E., Paletzki, R.F., Feroze, M.W., Eastwood, B.S., Couey, J.J., Winnubst, J., Chandrashekar, J., and Gerfen, C.R. (2018). Topographic precision in sensory and motor corticostriatal projections varies across cell type and cortical area. Nat. Commun. *9*, 3549.

Hrvatin, S., Hochbaum, D.R., Nagy, M.A., Cicconet, M., Robertson, K., Cheadle, L., Zilionis, R., Ratner, A., Borges-Monroy, R., Klein, A.M., et al. (2018). Single-cell analysis of experience-dependent transcriptomic states in the mouse visual cortex. Nat. Neurosci. *21*, 120–129.

Huerta-Ocampo, I., Mena-Segovia, J., and Bolam, J.P. (2014). Convergence of cortical and thalamic input to direct and indirect pathway medium spiny neurons in the striatum. Brain Struct. Funct. *219*, 1787–1800.

Hunnicutt, B.J., Jongbloets, B.C., Birdsong, W.T., Gertz, K.J., Zhong, H., and Mao, T. (2016). A comprehensive excitatory input map of the striatum reveals novel functional organization. eLife *5*, 9497.

Jeong, M., Kim, Y., Kim, J., Ferrante, D.D., Mitra, P.P., Osten, P., and Kim, D. (2016). Comparative three-dimensional connectome map of motor cortical projections in the mouse brain. Sci. Rep. *6*, 20072.

Jones, E.G. (2007). The Thalamus (Cambridge University Press).

Kato, S., Kuramochi, M., Kobayashi, K., Fukabori, R., Okada, K., Uchigashima, M., Watanabe, M., Tsutsui, Y., and Kobayashi, K. (2011). Selective neural pathway targeting reveals key roles of thalamostriatal projection in the control of visual discrimination. J. Neurosci. *31*, 17169–17179.

Kim, Y., Venkataraju, K.U., Pradhan, K., Mende, C., Taranda, J., Turaga, S.C., Arganda-Carreras, I., Ng, L., Hawrylycz, M.J., Rockland, K.S., et al. (2015). Mapping social behavior-induced brain activation at cellular resolution in the mouse. Cell Rep. *10*, 292–305.

Kim, E.J., Jacobs, M.W., Ito-Cole, T., and Callaway, E.M. (2016). Improved monosynaptic neural circuit tracing using engineered rabies virus glycoproteins. Cell Rep. *15*, 692–699.

Klein, S., Staring, M., Murphy, K., Viergever, M.A., and Pluim, J.P.W. (2010). elastix: a toolbox for intensity-based medical image registration. IEEE Trans. Med. Imaging *29*, 196–205.

Klein, A.M., Mazutis, L., Akartuna, I., Tallapragada, N., Veres, A., Li, V., Peshkin, L., Weitz, D.A., and Kirschner, M.W. (2015). Droplet barcoding for single-cell transcriptomics applied to embryonic stem cells. Cell *161*, 1187–1201.

Krashes, M.J., Shah, B.P., Madara, J.C., Olson, D.P., Strochlic, D.E., Garfield, A.S., Vong, L., Pei, H., Watabe-Uchida, M., Uchida, N., et al. (2014). An excitatory paraventricular nucleus to AgRP neuron circuit that drives hunger. Nature *507*, 238–242.

Lein, E.S., Hawrylycz, M.J., Ao, N., Ayres, M., Bensinger, A., Bernard, A., Boe, A.F., Boguski, M.S., Brockway, K.S., Byrnes, E.J., et al. (2007). Genome-wide atlas of gene expression in the adult mouse brain. Nature *445*, 168–176.

Lim, B.K., Huang, K.W., Grueter, B.A., Rothwell, P.E., and Malenka, R.C. (2012). Anhedonia requires MC4R-mediated synaptic adaptations in nucleus accumbens. Nature *487*, 183–189.

Macpherson, T., Morita, M., and Hikida, T. (2014). Striatal direct and indirect pathways control decision-making behavior. Front. Psychol. *5*, 1301.

Matsumoto, N., Minamimoto, T., Graybiel, A.M., and Kimura, M. (2001). Neurons in the thalamic CM-Pf complex supply striatal neurons with information about behaviorally significant sensory events. J. Neurophysiol. *85*, 960–976.

Minamimoto, T., Hori, Y., and Kimura, M. (2005). Complementary process to response bias in the centromedian nucleus of the thalamus. Science *308*, 1798–1801.

Miyamichi, K., Shlomai-Fuchs, Y., Shu, M., Weissbourd, B.C., Luo, L., and Mizrahi, A. (2013). Dissecting local circuits: parvalbumin interneurons underlie broad feedback control of olfactory bulb output. Neuron *80*, 1232–1245.

Nelson, A.B., and Kreitzer, A.C. (2014). Reassessing models of basal ganglia function and dysfunction. Annu. Rev. Neurosci. *37*, 117–135.

Oh, S.W., Harris, J.A., Ng, L., Winslow, B., Cain, N., Mihalas, S., Wang, Q., Lau, C., Kuan, L., Henry, A.M., et al. (2014). A mesoscale connectome of the mouse brain. Nature *508*, 207–214.

Osakada, F., and Callaway, E.M. (2013). Design and generation of recombinant rabies virus vectors. Nat. Protoc. *8*, 1583–1601.

Parent, M., and Parent, A. (2005). Single-axon tracing and three-dimensional reconstruction of centre median-parafascicular thalamic neurons in primates. J. Comp. Neurol. *481*, 127–144.

Parker, P.R.L., Lalive, A.L., and Kreitzer, A.C. (2016). Pathway-specific remodeling of thalamostriatal synapses in parkinsonian mice. Neuron *89*, 734–740.

Penney, J.B., Jr., and Young, A.B. (1983). Speculations on the functional anatomy of basal ganglia disorders. Annu. Rev. Neurosci. *6*, 73–94.

Peppe, A., Gasbarra, A., Stefani, A., Chiavalon, C., Pierantozzi, M., Fermi, E., Stanzione, P., Caltagirone, C., and Mazzone, P. (2008). Deep brain stimulation of CM/PF of thalamus could be the new elective target for tremor in advanced Parkinson's Disease? Parkinsonism Relat. Disord. *14*, 501–504.

Pert, C.B., Kuhar, M.J., and Snyder, S.H. (1976). Opiate receptor: autoradiographic localization in rat brain. Proc. Natl. Acad. Sci. USA *73*, 3729–3733.

Phillips, J.W., Schulmann, A., Hara, E., Liu, C., Wang, L., Shields, B., Korff, W., Lemire, A., Dudman, J., Nelson, S.B., et al. (2018). A single spectrum of neuronal identities across thalamus. bioRxiv. https://doi.org/10.1101/241315.

Plotkin, J.L., Day, M., and Surmeier, D.J. (2011). Synaptically driven state transitions in distal dendrites of striatal spiny neurons. Nat. Neurosci. *14*, 881–888.

Ragan, T., Kadiri, L.R., Venkataraju, K.U., Bahlmann, K., Sutin, J., Taranda, J., Arganda-Carreras, I., Kim, Y., Seung, H.S., and Osten, P. (2012). Serial two-photon tomography for automated ex vivo mouse brain imaging. Nat. Methods *9*, 255–258.

Raymond, C.S., and Soriano, P. (2007). High-efficiency FLP and PhiC31 site-specific recombination in mammalian cells. PLoS ONE *2*, e162.

Reiner, A., Medina, L., and Veenman, C.L. (1998). Structural and functional evolution of the basal ganglia in vertebrates. Brain Res. Brain Res. Rev. *28*, 235–285.

Robinson, R.B., and Siegelbaum, S.A. (2003). Hyperpolarization-activated cation currents: from molecules to physiological function. Annu. Rev. Physiol. *65*, 453–480.

Saalmann, Y.B. (2014). Intralaminar and medial thalamic influence on cortical synchrony, information transmission and cognition. Front. Syst. Neurosci. *8*, 83.

Saalmann, Y.B., Pinsk, M.A., Wang, L., Li, X., and Kastner, S. (2012). The pulvinar regulates information transmission between cortical areas based on attention demands. Science *337*, 753–756.

Sadikot, A.F., and Rymar, V.V. (2009). The primate centromedian-parafascicular complex: anatomical organization with a note on neuromodulation. Brain Res. Bull. *78*, 122–130.

Satija, R., Farrell, J.A., Gennert, D., Schier, A.F., and Regev, A. (2015). Spatial reconstruction of single-cell gene expression data. Nat. Biotechnol. *33*, 495–502.

Saunders, A., Johnson, C.A., and Sabatini, B.L. (2012). Novel recombinant adeno-associated viruses for Cre activated and inactivated transgene expression in neurons. Front. Neural Circuits *6*, 47.

Saunders, A., Oldenburg, I.A., Berezovskii, V.K., Johnson, C.A., Kingery, N.D., Elliott, H.L., Xie, T., Gerfen, C.R., and Sabatini, B.L. (2015). A direct GABAergic output from the basal ganglia to frontal cortex. Nature *521*, 85–89.

Saunders, A., Huang, K.W., and Sabatini, B.L. (2016). Globus pallidus externus neurons expressing parvalbumin interconnect the subthalamic nucleus and striatal interneurons. PLoS ONE *11*, e0149798.

Savitzky, A., and Golay, M.J.E. (1964). Smoothing and differentiation of data by simplified least squares procedures. Anal. Chem. *36*, 1627–1639.

Schindelin, J., Arganda-Carreras, I., Frise, E., Kaynig, V., Longair, M., Pietzsch, T., Preibisch, S., Rueden, C., Saalfeld, S., Schmid, B., et al. (2012). Fiji: an open-source platform for biological-image analysis. Nat. Methods *9*, 676–682.

Sherman, S.M. (2016). Thalamus plays a central role in ongoing cortical functioning. Nat. Neurosci. *19*, 533–541.

Sherman, S.M., and Guillery, R.W. (2013). Functional Connections of Cortical Areas (MIT Press).

Smeal, R.M., Gaspar, R.C., Keefe, K.A., and Wilcox, K.S. (2007). A rat brain slice preparation for characterizing both thalamostriatal and corticostriatal afferents. J. Neurosci. Methods *159*, 224–235.

Smith, Y., and Parent, A. (1986). Differential connections of caudate nucleus and putamen in the squirrel monkey (Saimiri sciureus). Neuroscience *18*, 347–371.

Smith, Y., Galvan, A., Ellender, T.J., Doig, N., Villalba, R.M., Huerta-Ocampo, I., Wichmann, T., and Bolam, J.P. (2014). The thalamostriatal system in normal and diseased states. Front. Syst. Neurosci. *8*, 5.

Steiner, H., and Tseng, K.Y. (2016). Handbook of Basal Ganglia Structure and Function (Academic Press).

Stephenson-Jones, M., Samuelsson, E., Ericsson, J., Robertson, B., and Grillner, S. (2011). Evolutionary conservation of the basal ganglia as a common vertebrate mechanism for action selection. Curr. Biol. *21*, 1081–1091.

Straub, C., Tritsch, N.X., Hagan, N.A., Gu, C., and Sabatini, B.L. (2014). Multiphasic modulation of cholinergic interneurons by nigrostriatal afferents. J. Neurosci. *34*, 8557–8569.

Sunkin, S.M., Ng, L., Lau, C., Dolbeare, T., Gilbert, T.L., Thompson, C.L., Hawrylycz, M., and Dang, C. (2013). Allen Brain Atlas: an integrated spatio-temporal portal for exploring the central nervous system. Nucleic Acids Res. *41*, D996–D1008.

Tervo, D.G.R., Hwang, B.-Y., Viswanathan, S., Gaj, T., Lavzin, M., Ritola, K.D., Lindo, S., Michael, S., Kuleshova, E., Ojala, D., et al. (2016). A designer AAV variant permits efficient retrograde access to projection neurons. Neuron *92*, 372–382.

Testini, P., Min, H.-K., Bashir, A., and Lee, K.H. (2016). Deep brain stimulation for Tourette's syndrome: the case for targeting the thalamic centromedian-parafascicular complex. Front. Neurol. *7*, 193.

Trapnell, C., Cacchiarelli, D., Grimsby, J., Pokharel, P., Li, S., Morse, M., Lennon, N.J., Livak, K.J., Mikkelsen, T.S., and Rinn, J.L. (2014). The dynamics and regulators of cell fate decisions are revealed by pseudotemporal ordering of single cells. Nat. Biotechnol. *32*, 381–386.

Wall, N.R., De La Parra, M., Callaway, E.M., and Kreitzer, A.C. (2013). Differential innervation of direct- and indirect-pathway striatal projection neurons. Neuron *79*, 347–360.

Wallace, M.L., Saunders, A., Huang, K.W., Philson, A.C., Goldman, M., Macosko, E.Z., McCarroll, S.A., and Sabatini, B.L. (2017). Genetically distinct

parallel pathways in the entopeduncular nucleus for limbic and sensorimotor output of the basal ganglia. Neuron *94*, 138–152.e5.

Wickersham, I.R., Lyon, D.C., Barnard, R.J.O., Mori, T., Finke, S., Conzelmann, K.K., Young, J.A.T., and Callaway, E.M. (2007). Monosynaptic restriction of transsynaptic tracing from single, genetically targeted neurons. Neuron *53*, 639–647.

Wickersham, I.R., Sullivan, H.A., and Seung, H.S. (2010). Production of glycoprotein-deleted rabies viruses for monosynaptic tracing and high-level gene expression in neurons. Nat. Protoc. *5*, 595–606.

Zilionis, R., Nainys, J., Veres, A., Savova, V., Zemmour, D., Klein, A.M., and Mazutis, L. (2017). Single-cell barcoding and sequencing using droplet microfluidics. Nat. Protoc. *12*, 44–73.

STAR★METHODS

KEY RESOURCES TABLE

REAGENT or RESOURCE	SOURCE	IDENTIFIER
Antibodies		
Rabbit polyclonal anti-OPRM1	Millipore	Cat# AB5511; RRID: AB_177512
Goat anti-rabbit IgG secondary antibody, Alexa 594 conjugate	Thermo Fisher Scientific	Cat# R37117; RRID: AB_2556545
Goat anti-rabbit IgG secondary antibody, Alexa 647 conjugate	Thermo Fisher Scientific	Cat# A32733; RRID: AB_2633282
Bacterial and Virus Strains		
B19G-SADΔG-H2B:EGFP (RV-nGFP)	Plasmid: this paper. Production: Sabatini Lab, Wickersham et al., 2010	N/A
B19G-SADΔG-EGFP (RV-GFP)	Plasmid: Byungkook Lim, Lim et al., 2012 Production: Sabatini Lab, Wickersham et al., 2010.	N/A
B19G-SADΔG-ChR2-EYFP (RV-ChR2)	Plasmid: Byungkook Lim, Lim et al., 2012 Production: Sabatini Lab, Wickersham et al., 2010.	N/A
EnvA-SADΔG-EGFP (p.RV-GFP)	Plasmid: Byungkook Lim, Lim et al., 2012 Production: Sabatini Lab, Wickersham et al., 2010	N/A
Chemicals, Peptides, and Recombinant Proteins		
Cholera Toxin Subunit B (Recombinant), Alexa Fluor 488 Conjugate,	Thermo Scientific; Conte et al., 2009	Cat# C22841
Cholera Toxin Subunit B (Recombinant), Alexa Fluor 555 Conjugate	Thermo Scientific; Conte et al., 2009	Cat# C22843
Cholera Toxin Subunit B (Recombinant), Alexa Fluor 647 Conjugate,	Thermo Scientific; Conte et al., 2009	Cat# C34778
Critical Commercial Assays		
RNAscope Multiplex FluorescentReagent Kit	Advanced Cell Diagnostics	Cat# 320850
Deposited Data		
Reagent or Resource: Data files for RNA sequencing	Source: This paper	Identifier: GEO: GSE128393
Experimental Models: Organisms/Strains		
Mouse: C57BL/6NCrl	Charles River	cat# 027
Mouse: Pdyn-IRES-Cre, B6;129S-Pdyn$^{tm1.1(cre)Mjkr}$/LowlJ	Jackson Laboratories	cat# 027958
Mouse: Rbp4-Cre, B6.FVB(Cg)-Tg(Rbp4-cre) KL100Gsat/Mmucd	GENSAT; Gong et al., 2007	Cat# KL100; RRID: MMRRC_037128-UCD
Mouse: LHX6-EGFP, Tg(Lhx6EGFP) BP221Gsat/Mmmh	GENSAT; Gong et al., 2007	Cat# 000246-MU RRID: MMRRC_000246-MU
Recombinant DNA		
AAV2/8-EF1a-FAS-TdTomato-WPRE-pA	UNC viral vector core, Saunders et al., 2012	Addgene# 37092
AAV2/8-EF1a-DIO-EGFP-WPRE-pA	UNC viral vector core, Saunders et al., 2012	Addgene# 37084
AAV2/8-EF1a-DIO-hChR2(H134R)-mCherry-WPRE-HGHpA	UNC viral vector core	Addgene# 20297; RRID: Addgene_20297
AAV2/8-EF1a-DIO-hChR2(H134R)-EYFP-WPRE-HGHpA	UNC viral vector core	Addgene# 20298; RRID: Addgene_20298

(*Continued on next page*)

Continued

REAGENT or RESOURCE	SOURCE	IDENTIFIER
AAV1-CAG-FLEX-tdTomato-WPRE-bGHpA	Penn Vector Core, Oh et al., 2014	Addgene# 51503; RRID: Addgene_51503
AAV1-CAG-FLEX-EGFP-WPRE-bGHpA	Penn Vector Core, Oh et al., 2014	Addgene# 51502; RRID: Addgene_51502
AAV2/9-CAG-FLEx-TVA(TCB)-mCherry	Boston Children Hospital Vector Core, Miyamichi et al., 2013	Addgene# 48332; RRID: Addgene_48332
AAV2/9-CAG-FLEX-oG-WPRE-SV40pA	Boston Children Hospital Vector Core, Kim et al., 2016	Addgene# 74292; RRID: Addgene_74292
AAV/DJ-hSyn Coff/FonEYFP	UNC viral vector core	Addgene# 55652; RRID: Addgene_55652
AAV2rg-EF1a-Cre	Boston Children Hospital Vector Core, Tervo et al., 2016	Addgene# 55636; RRID: Addgene_55636
AAV2rg-EF1a-FlpO-WPRE	Boston Children Hospital Vector Core, Raymond and Soriano, 2007; Tervo et al., 2016	Addgene# 13793; RRID: Addgene_13793
Software and Algorithms		
FIJI	NIH; Schindelin et al., 2012	https://imagej.net/Fiji, RRID: SCR_00228
MATLAB	MathWorks	https://www.mathworks.com/products/matlab.html?s_tid=hp_products_matlab; RRID: SCR_001622
Jupyter Notebook	https://jupyter.org/	N/A
GraphPad Prism 6,7,8	GraphPad Software	https://www.graphpad.com/; RRID: SCR_002798
Imaris, version 9.2	Bitplane	http://www.bitplane.com/imaris/imaris; RRID: SCR_007370
Code for STPT	Kim et al., 2015	https://www.ncbi.nlm.nih.gov/pubmed/25558063
Other		
In drops reagents	Klein et al., 2015	N/A

CONTACT FOR REAGENT AND RESOURCE SHARING

Further information and requests for reagents may be directed to, and will be fulfilled by, the lead contact Bernardo L. Sabatini (bernardo_sabatini@hms.harvard.edu).

EXPERIMENTAL MODEL AND SUBJECT DETAILS

Mice

This study is based on data from mice at postnatal day 50 and includes both males and females. We used C57BL/6NCrl mice (Charles River Laboratories, Wilmington, MA, stock #027) as well as the following transgenic lines: B6;129S-*Pdyn*$^{tm1.1(cre)Mjkr}$/LowlJ (*Dyn-IRES-cre)* (Jackson Laboratories, Bar Harbor, ME, stock #027958), *Tg(Rbp4-cre)KL100Gsat* mice (*Rbp4-Cre*) (Gensat project, founder line KL100), and *Tg(Lhx6-EGFP)BP221Gsat* (*LHX6-EGFP)* Gensat project, founder line BP221). Animals were maintained on a C57BL/6 background and kept on a 12:12 light/dark cycle or a reversed cycle under standard housing conditions. Experimental manipulations were performed in accordance with protocols approved by the Harvard Standing Committee on Animal Care following guidelines described in the US National Institutes of Health Guide for the Care and Use of Laboratory Animals. All mice brain coordinates in this study are given with respect to Bregma; anterior–posterior (A/P), medial–lateral (M/L), and dorsal–ventral (D/V).

METHOD DETAILS

AAVs

Recombinant adeno-associated viruses (AAVs of serotype 1,2,8,9 or DJ) encoding a double floxed inverted (DFI) gene under the control of CAG, EF1a, or hSyn promoters were used to express the transgene of interest in the Cre-recombinase expressing neurons. Retrograde AAVs that efficiently infect axons (Tervo et al., 2016) were used to deliver Flp (Raymond and Soriano, 2007) or Cre recombinase to neurons upstream of the injection site. Additionally, we used intersectional AAVs that expressed the transgene only when Flp is present and Cre is absent (FlpOn/CreOff). AAVs were packaged by commercial vector core facilities (UNC Vector Core, Penn

Vector Core, Boston Children's Hospital Vector Core) and upon arrival stored at a working concentration (10^{11} to 10^{13} genomic copies per ml) at −80°C.

Rabies viruses

Rabies viruses carrying the transgene for the H2B:EGFP fusion protein were generated in-house. Synthesized H2B-EGFP vector was cloned into pSPBN-SADΔG-tdTomato plasmid using SmaI and NheI restriction sites, replacing the tdTomato sequence. B19G-SADΔG-H2B:EGFP virions were first generated via cDNA rescue using a procedure based on previously described protocols (Wickersham et al., 2010). HEK293T cells (ATCC CRL-11268) were transfected with pSPBN-SADΔG-H2B:EGFP, pTIT-B19N, pTIT-B19P, pTIT-B19G, pTIT-B19L and pCAGGS-T7 using the Lipofectamine 2000 transfection reagent. 5 to 7 days post-transfection, the supernatant was filtered through a 0.22 μm PES filter and transferred to BHK-B19G cells for amplification. Virions were then serially amplified in three rounds of low-MOI passaging through BHK-B19G cells by transfer of filtered supernatant, with 3 to 4 days between passages. Cells were grown at 35°C and 5% CO_2 in DMEM with GlutaMAX (Thermo Scientific, #10569010) supplemented with 5% heat-inactivated FBS (Thermo Scientific #10082147) and antibiotic-antimycotic (Thermo Scientific #15240-062). For concentrating the virions, media from dishes containing virion-generating cells was first collected and incubated with benzonase nuclease (1:1000, Millipore #70664) at 37°C for 30 min before filtering through a 0.22 μm PES filter. The filtered supernatant was transferred to ultracentrifuge tubes (Beckman Coulter #344058) with 2 mL of a 20% sucrose in dPBS cushion and ultracentrifugated at 20,000 RPM (Beckman Coulter SW 32 Ti rotor) at 4°C for 2 h. The supernatant was discarded and the pellet was re-suspended in dPBS for 6 h on an orbital shaker at 4°C before aliquots were prepared and frozen for long-term storage at −80°C. Unpseudotyped rabies virus titers were estimated based on a serial dilution method (Osakada and Callaway, 2013) counting infected (H2B:EGFP$^+$) HEK293T cells, and quantified as infectious units per ml (IU/ml). B19G-SADΔG-EGFP, EnvA-SADΔG-EGFP, and B19G-SADΔG-ChR2-EYFP viruses were generated by amplification from existing in-house stocks using similar passaging procedures described above. Pseudotyping was performed after the last passaging round of unpseudotyped virion amplification. BHK-EnvA cells were infected with the filtered supernatant containing unpseudotyped virions for 6 h, followed by two rounds of trypsinization with dPBS washes and re-plating over two consecutive days. Pseudotyped rabies virus titers were estimated as described above counting infected (EGFP$^+$) HEK293T-TVA800 cells. For quality control, pseudotyped rabies virus stocks were tested *in vitro* for leak of unpseudotyped virus with a similar titering protocol by infecting HEK293T cells. Virus batches used had a leak of less than 2×10^3 IU/ml. Starting materials for rabies viruses were generously provided by Byungkook Lim (UCSD) (Lim et al., 2012).

Stereotaxic Intracranial Injections

Mice were anesthetized with 2.5% isoflurane in 80% oxygen and placed in a stereotaxic frame (David Kopf Instruments Model 900). Under aseptic conditions, the skull was exposed and leveled (< 100 μm difference between 1.5+A/P and Lambda as a cutoff for proper leveling of the skull). 250 μm craniotomies were made with an electric drill (Foredom Electric Company K.1070) with a ball bur (Busch and Co. S33289) attached to the manipulator. All reagents were injected through a pulled glass pipette (Drummond Scientific Company pipettes) with a tip of approximate 50 μm (pulled with a P-97 model Sutter Instrument Co. pipette puller). To avoid leak into other brain regions and back spill through the pipette track the injection pipette was lowered 200 μm ventral to the region of injection before being brought up to the point of injection. The pipette was left in place for 3min prior to injection and the reagent of interest was delivered at a rate of 50nl/min using a UMP3 micro-syringe pump (World Precision Instruments). Following injection, we waited 5min at the injection site before raising the pipette 200 μm above the injection site and then waited an additional 5 min before retracting the pipette from the brain at ~1mm/min. To minimize their dehydration during surgery mice received a subcutaneous injection of 1ml of sterile saline (Teknova S5819). Additionally, in order to reduce inflammation, mice received an injection of Ketoprofen (Zoetis 07-803-7389) at an amount of 0.01mg per gram of animal mass. Postoperatively, mice were monitored on a heat pad for 1 h before being returned to their home cage. Mice were then monitored daily for at least 5 days and received a MediGel Carprofen cup in their home cage (Clear H_2O).

Injection coordinates

All coordinates that were used in this study were relative to Bregma (in mm) and were: for PFC: 2.8 A/P, 1.2 M/L, 0.9 D/V; MOs: 0.8, 0.9, both 0.8 and 0.5; SSp: 1.0, 2.2, 1.0; mSTR: 0.8, 1.0, both 3.3 and 2.7; dmSTR: 0.8, 1.6, 2.6; dlSTR: 0.8, 2.4, 2.5; ACB: 0.8, 1.5, 4.6; mPF: −2.1, 0.5, both 3.7 and 3.5; lPF: −2.1, 0.88, both 3.75 and 3.55.

Injection volumes and waiting time for specific anatomical regions and reagents

The injection volumes by region and reagent were (in nl): mSTR: RV-nGFP (150-200), CTB (80-200); dmSTR: RV-nGFP (150-200), CTB (80-200), retro-Flp (200), retro-Cre (300), RV-GFP (100), RV-ChR2 (200); dLSTR: RV-nGFP(150-200), CTB (80-200), retro-Flp (200), retro-Cre (300), RV-GFP (100), RV-ChR2 (200); mPF: CreOn-GFP (75-150), CreOn-ChR2-mCherry (200-300), CreOn-ChR2-GFP (200-300), CreOff/FlpOn-GFP (200), CreOn-TVA (100), CreOn-OG (100), p.RV-GFP (150-200); LPF: CreOff/FlpOn-GFP (200), CreOn-ChR2-mCherry (200-400); ACB: CTB (80-140); MOs: CreOn-GFP (200), CreOn-ChR2-GFP (250); SSp: CreOn-GFP (200), CreOn-TdTom (200), CreOn-ChR2-mCherry (100-250); PFC: CreOn-GFP (200-250), CreOn-TdTom (200-250), CreOn-ChR2-GFP (100-250). Waiting times for reagents were as follows: CTB: 3-7 days; AAVs: 2.5-5 weeks; RV-nGFP: 5-10 days; RV-EGFP: 7-10 days. RV-ChR2: 3-7 days; p.RV-GFP: 5-10 days;

Histology and Imaging for STPT

Animals were perfused transcardially with ice-cold 0.9% saline solution followed by 4% paraformaldehyde (PFA) (diluted in 0.2 M phosphate buffer) for 7 min at 7 ml/min. Brain were fixed in 4% PFA for 24h before being transferred to 0.1 M glycine solution (diluted 0.1 M phosphate buffer), for 48h at 4°C before being stored in 0.1 M phosphate buffer at 4°C until imaged. Imaging was done as previously described (Ragan et al., 2012). Brains were embedded in 4% agarose in 0.05M PB, cross-linked in 0.2% sodium borohydrate solution (in 0.05 M sodium borate buffer, pH 9.0-9.5). The entire brain (including the olfactory bulb and the cerebellum) was imaged with a high-speed 2-photon microscope with integrated vibratome at 1 μm-1 μm x-y resolution with spacing of 50 μm on a TissueCyte 1000 (TissueVision). The 2-photon excitation wavelength was 910 nm, which efficiently excites GFP. A 560 nm dichroic mirror (Chroma, T560LPXR) and band pass filters (Semrock FF01-520/35 an) were used to separate green.

Histology and imaging for all other experiments

Mice were anesthetized with isoflurane and perfused transcardially with 4% PFA in 0.1 M sodium phosphate buffer (PBS). Brains were post-fixed for 24-48 h and transferred to a 0.1 M PBS solution until further processing. Coronal slices (50 μm thickness) were cut with a vibrating blade microtome (Leica Biosystems VT1000S). Brain sections were mounted on superfrost slides (VWR 48311-703) dried, and coverslipped with ProLong antifade reagent containing DAPI (Thermo Scientific Cat# P36962). Whole slides were imaged with an Olympus VS120 slide-scanning microscope with a 10X objective. Specific regions of interest were imaged with a Leica SPX8 confocal microscope using a 10X or 60X objectives at the Harvard Neurobiology Imaging Facility and Harvard Neurodiscovery Imaging Core.

Immunohistochemistry

Slices were rinsed 3 times for 5 min in PBS before being incubated in PBS blocking solution containing 0.3% Triton X-100 (PBST) for 1h at RT (20–22°C). Slices were then incubated over night at 4°C in the same blocking solution with 1% goat serum and MOR rabbit polyclonal primary antibody (Millipore Cat# AB5511). The next day, slices were rinsed 3 × 10 min in PBS before being incubated in the blocking solution with 1 mg/mL goat anti-rabbit conjugated with Alexa Fluor 594 or Alexa Fluor 647 secondary antibody (Thermo Scientific Cat# R37117 and Cat# A32733, respectively). The slices were then rinsed again, mounted, and imaged as described above in the ''histology and imaging for all other experiment'' section.

In situ hybridization

Tissue for *in situ* hybridization was processed using a previously described protocol (Hrvatin et al., 2018) and according to the ACD RNAscop Fluorescent Multiple Assay manual. Animals were euthanized and brains were immediately frozen on dry ice to be sliced via cryostat (Leica CM 1950). For the image presentation of the ISH in Figure 3, nuclei masks were created and each nucleus was pseudo-colored according to the number of puncta contained within the specific mask, as previously described (Hrvatin et al., 2018).

Whole-cell dissociation and RNA capture

Dissociated whole-cell suspensions were prepared using a protocol adapted from Hrvatin et al. (2018). 8-week old C57BL/6NCrl male mice (Charles River Laboratories, Wilmington, MA, stock #027) were pair-housed for a few days after arrival in a regular light/dark cycle room prior to tissue collection. Mice were transcardially perfused with an ice-cold choline cutting solution containing neuronal activity blockers (110 mM choline chloride, 25 mM sodium bicarbonate, 12 mM D-glucose, 11.6 mM sodium L-ascorbate, 10 mM HEPES, 7.5 mM magnesium chloride, 3.1 mM sodium pyruvate, 2.5 mM potassium chloride, 1.25 mM sodium phosphate monobasic, 10 μM (R)-CPP, 1 μM tetrodotoxin, saturated with bubbling 95% oxygen/5% carbon dioxide, pH adjusted to 7.4 using sodium hydroxide). Brains were rapidly dissected out and sliced into 250 μm thick coronal sections on a Leica VT1000 vibratome in a chilled cutting chamber filled with choline cutting solution. Coronal slices containing the TH were then transferred to a chilled dissection dish containing choline cutting solution for microdissection of the PF under a stereomicroscope. Dissected tissue chunks were transferred to cold HBSS-based dissociation media (Thermo Scientific Cat. # 14170112, supplemented to final content concentrations: 138 mM sodium chloride, 11 mM D-glucose, 10 mM HEPES, 5.33 mM potassium chloride, 4.17 mM sodium bicarbonate, 2.12 mM magnesium chloride, 0.9 mM kynurenic acid, 0.441 mM potassium phosphate monobasic, 0.338 mM sodium phosphate monobasic, 10 μM (R)-CPP, 1 μM tetrodotoxin, saturated with bubbling 95% oxygen/5% carbon dioxide, pH adjusted to 7.35 using sodium hydroxide) supplemented with an additional inhibitor cocktail (10 μM triptolide, 5 μg/ml actinomycin D, 30 μg/ml anisomycin) and kept on ice until dissections were completed. The remaining tissue was fixed in 4% PFA in PBS for histological verification. Dissected tissue chunks from 8 mice were pooled into a single sample for the subsequent dissociation steps. Tissue chunks were first mixed with a digestion cocktail (dissociation media, supplemented to working concentrations: 20 U/ml papain, 1 mg/ml pronase, 0.05 mg/mL DNase I, 10 μM triptolide, 5 μg/ml actinomycin D, 30 μg/ml anisomycin) and incubated at 34°C for 90 min with gentle rocking. The digestion was quenched by adding dissociation media supplemented with 0.2% BSA and 10 mg/ml ovomucoid inhibitor (Worthington Cat. # LK003128), and samples were kept chilled for the rest of the dissociation procedure. Digested tissue was collected by brief centrifugation (5 min, 300 *g*), re-suspended in dissociation media supplemented with 0.2% BSA, 1 mg/ml ovomucoid inhibitor, and 0.05 mg/mL DNase I. Tissue chunks were then mechanically triturated using fine-tip plastic micropipette tips of progressively decreasing size. The triturated cell suspension was filtered in two stages using a 70 μm cell strainer (Miltenyi Biotec Cat # 130-098-462) and 40 μm pipette tip filter (Bel-Art Cat. # H136800040) and washed in two repeated centrifugations

(5 min, 300 *g*) and re-suspension steps to remove debris before a final re-suspension in dissociation media containing 0.04% BSA and 15% OptiPrep (Sigma D1556). Cell density was calculated based on hemocytometer counts and adjusted to approximately 100,000 cells/ml. Single-cell encapsulation and RNA capture on the inDrop platform was performed at the Harvard Medical School ICCB Single Cell Core using v3 chemistry hydrogels based on previously described protocols (Zilionis et al., 2017). Suspensions were kept chilled until the cells were flowed into the microfluidic device. The encapsulated droplets were broken and cDNA was processed for next-gen sequencing, as previously described (Klein et al., 2015) generating index libraries that were then pooled and sequenced across 3 runs on the NextSeq500 (Illumina) platform.

Acute Brain Slice Preparation and Whole-Cell Recordings

Experiments were done as previously described (Saunders et al., 2015; Wallace et al., 2017) with few modifications. Mice were anesthetized by isoflurane inhalation and perfused transcardially with ice-cold artificial cerebrospinal fluid (ACSF) containing (in mM) 125 NaCl, 2.5 KCl, 25 $NaHCO_3$, 2 $CaCl_2$, 1 $MgCl_2$, 1.25 NaH_2PO_4 and 11 glucose (300-305 mOsm/kg) at a rate of 12ml/min for 1 to 2 min. 250 or 300 μm coronal slices were cut in ice-cold ACSF and transferred for 10 min to a holding chamber at 34°C containing choline-based solution consisting of (in mM): 110 choline chloride, 25 NaHCO3, 2.5 KCl, 7 MgCl2, 0.5 CaCl2, 1.25 NaH2PO4, 25 glucose, 11.6 ascorbic acid, and 3.1 pyruvic acid before transferring to a second 34°C temperature chamber with ACSF for at least 30 min. After 30 min the chamber was moved to room temperature for the duration of the experiment. Recordings were performed at 32°C with a flow of 2-3ml/min carbogen-bubbled ACSF. We used patch pipettes (2.5–3.5 MΩ) pulled from borosilicate glass (Sutter Instruments). Cs-based internals for voltage-clamp measurements (in mM: 135 $CsMeSO_3$, 10 HEPES, 1 EGTA, 3.3 QX-314 (Cl^- salt), 4 Mg-ATP, 0.3 Na-GTP, 8 Na_2-Phosphocreatine, pH 7.3 adjusted with CsOH; 295 mOsm·kg^{-1}) and K-based internals for current-clamp measurements (in mM: 135 $KMeSO_3$, 3 KCl, 10 HEPES, 1 EGTA, 0.1 $CaCl_2$, 4 Mg-ATP, 0.3 Na-GTP, 8 Na_2-Phosphocreatine, pH 7.3 adjusted with KOH; 295 mOsm·kg^{-1}). FSIs, LTSIs in the LHX6-GFP mice were first identified based on fluorescence. FSIs, LTSIs, TANs and SPNs were all identified based on responses to current injections, membrane resistance, and the presence or absence of dendritic spines as previously described in Saunders et al. (2016) and Straub et al. (2014). For optogenetics experiments, 3 to 5 ms duration light pulses from a 473 nm laser (5-10mW per mm^2 measured at the sample plane) were used.

PF subregion targeting strategies used in Figure 6

For mPF, Cre-dependent AAV was injected directly into PF to express GFP in *Pdyn* neurons. For cPF, axon-infecting AAV encoding Flp recombinase was injected in dmSTR and AAV that expresses GFP in the presence of Flp and absence of Cre was injected into PF. A similar approach was used for lPF, with injection of axon-infecting AAV-Flp into dlSTR. These strategies succeeded in largely restricting GFP expression to the targeted subregion and to the anterior-posterior extent of PF (% cells in PF when targeting mPF = 83% ± 3%, n = 2696/3; cPF = 58% ± 3%, n = 8069/4; lPF = 80% ± 5%, n = 7132/5 cells/mice; Figure S6A).

QUANTIFICATION AND STATISTICAL ANALYSIS

General

Data points are stated and plotted as mean values ± SEM. All experiments with less than 24 data points are plotted showing all the data points. p values are represented by symbols using the following code: * for $0.01 < p < 0.05$, ** for $0.001 < p < 0.01$, and *** for $p < 0.001$. Exact p values and statistical tests are stated in figure legends. All statistical tests were non-parametric as noted. No *a priori* power analyses were done.

STPT cell count Image Analysis

Raw images were corrected for non-uniform illumination and stitched in 2D, and stacked in 3D. Nuclear GFP+ neurons were automatically detected by a convolutional network trained to recognize nuclear labeling. The 3D stack was then registered to a 3D reference brain based on the ABA (Kim et al., 2015; Sunkin et al., 2013) by 3D affine registration followed by a 3D B-spline registration using the software Elastix (Klein et al., 2010). The number of total input neurons in each brain region was normalized by the total number of GFP+ cells detected in the parent region (e.g., in Figure 1D the parent region is the sub-CTX).

Brain volume quantification

To measure the volume of anatomical regions, the average reference brain (built using 40 STPT imaged brains) was aligned to the ABA. Segmentation areas were registered onto each brain using the B-spline registration procedure described above (i.e., the ABA segmentation was registered onto each individual brain). The number of voxels belonging to each region in the transformed ABA segmentation were counted and multiplied by $0.02 \times 0.02 \times 0.05$ mm^3 (the dimensions of an anatomical voxel spacing unit), resulting in the total volume of each region.

Projection mapping data processing

Previously published methods were adopted for quantifying neuronal projections as imaged by STPT (Oh et al., 2014). Filtered images of the original image data were generated by applying a square root transformation, histogram matching to the original image, and median and Gaussian filtering using FIJI (NIH) (Schindelin et al.,2012) software. The original images were then subtracted from

the filtered images to generate signal images. These were then converted to binary maps by applying a threshold chosen to maximize signal retention while minimizing background auto-fluorescence. We cannot rule out the possibility that faint and sparse signals were being missed by the automated detection. False-positive signals at the injection sites and from bright fluorescence from the dura were removed using manually curated masks for each brain. The method measures fluorescence from all axons, including axons of passage. For this reason, we only analyzed signals in CTX, where fibers of passage are less likely. To calculate the putative output of PF to CTX the relative axon density was measured as the fraction of all GFP+ pixels that are located in a given area divided by the fraction of cortical volume contained in the area. This metric gives the relative enrichment of axons in each cortical area compared to a uniform distribution of axons within CTX. The scalable brain atlas (https://scalablebrainatlas.incf.org/) was used for Figures 6C–6H visualization (Bezgin et al., 2009). 3D reconstruction of the PF (Video S4) was done using Imaris version 9.2 (Bitplane). For this video, we combined the three samples that are shown in Figure 6 at 5% the resolution of the original STPT images

Image analysis for all other experiments

Quantification of the distribution of fluorescence of CTB+ across the medial lateral axis of PF (Figure 2) was done using a custom macro in FIJI (NIH). For each coronal section in PF, and based on the ABA, the mean pixel fluorescence was calculated across a ventral-dorsal line with a 0.6 μm medial-lateral width. Using Graph-Pad prism (GraphPad Software, La Jolla, CA), a 2nd order smoothing (Savitzky and Golay, 1964) was applied with 200 nearest neighbors prior to normalizing each channel. For the quantification of the distribution of CTB+ pixels across the anterior posterior axis of PF (Figure S2) was done using a custom macro in FIJI. A triangular thresholding method was applied and a Gaussian blur with radius of 3 pixels was used before calculating the number of positive pixels in each channel and each image. In Figures S2B and S2C the percentage of labeled pixels was calculated by dividing the labeled pixels in each section or subregion by the total number of labeled pixels in that mouse or coronal slice, respectively. To calculate the overlap between PF subregions (Figure S2D) we calculated the percentage of the positive pixels in each channel that were also positive in the other channels.

For quantification of the distribution of GFP fluorescence in PF and STR (Figure 4) the same analysis was used as in Figure 2, with the exception of the ventral dorsal line scan being 1.0mm wide. For analysis of *Pdyn*+ PF→STR axons coronal sections of STR at +0.6, +0.9, and +1.2 mm were grouped together. For the analysis of topographical organization of *Pdyn*+ axons in STR (Figure 4) patches (based on MOR stain) were manually labeled while being blinded to the GFP+ PF→STR axon location. Using a custom macro in FIJI each patch label was expanded by 100 μm in all directions and the mean fluorescence of the patch and this peri-patch region were calculated for the MOR channel and the axon channels. For image analysis of the Layer 5 CTX→PF inputs (Figure 7) the DAPI channel was used to manually mark the location of PF to ensure that the selection was done solely based on anatomical location as defined in Figure 1 and based on the ABA. The CTB channel was used to label the region in PF with all CTB+ cells and mean fluorescence was measured in the that region compared to the rest of PF (rPF) (Figure S7). Next, the areas define as encompassing the CTB+ cells in PF was applied to the CTX→PF axon channel and fluorescence of axons were calculated in that region and compared to the rest of PF. Background fluorescence was calculated by taking the mean of 3 random tissue areas of 0.3mm^2 each. The comparison of the fluorescence inputs from CTX to PF, IPSI to the injection sight versus CONTRA to the injection sight (Figure S8) was done by manually labeling the axons IPSI to the injection sight. The axon location CONTRA to the injections was at a similar location and shape as IPSI to the injection, allowing the IPSI side label to be reflected to the CONTRA side. Correction for background fluorescence was done as described above.

InDrops Analysis

Transcripts were processed according to a previously published pipeline (Klein et al., 2015; Hrvatin et al., 2018). A custom transcriptome was assembled from the Ensembl GRCm38 genome and GRCm38.84 annotation using Bowtie 1.1.1, after filtering the annotation gtf file (gencode.v17.annotation.gtf filtered for feature_type = ”gene,” gene_type = ”protein_coding” and gene_status = ”KNOWN”). Read quality control and mapping against this transcriptome was performed using default parameters. Unique molecular identifiers (UMIs) were used to reference sequence reads back to individual captured molecules. The output matrix (cells x genes) was then filtered to exclude cells with less than 500 UMIs and used as the input to the Seurat pipeline for further analysis (Satija et al., 2015). Genes were excluded if UMIs were found in 3 cells or less. Cells were excluded if they expressed fewer than 400 genes, or more than 5500 genes. Cells with 15% or more of their transcriptome derived from mitochondrial genes were excluded. Finally, cell doublets were estimated by creating synthetic doublets from the dataset and computing a k-nearest neighbor graph (k = 30) with both cells and synthetic doublets. Cells were ranked according to the percentage of nearest neighbors that were synthetic doublets. Cells in the top 5% of doublet scores were excluded as putative doublets. Transcript counts were scaled to 10,000 transcripts per cell and log-plus-one transformed. Variable genes were identified using the MeanVarPlot() function, which calculates the average expression and dispersion for each gene, then bins genes and calculates a z-score for dispersion within each bin. The following parameters were used to set the minimum and maximum average expression and the minimum dispersion: x.low.cutoff = 0.0125, x.high.cutoff = 3, y.cutoff = 0.5. Next, the count matrix was regressed against the number of UMIs and percentage of counts comprising mitochondrial genes and scaled. PCA was carried out and the top 20 principal components (PCs) were kept. Finally clustering was performed using the FindClusters() routine. Clustering resolution was set to 0.6. This resulted in 13 initial clusters, which were categorized into 7 broad cell-type classes by canonical gene expression patterns (Mrc1/Cd36 for macrophage, Olig1/Pdgfra for oligodendrocytes and oligodendrocyte precursors, Vtn for pericytes, Cldn5/Pecam1 for endothelial and smooth

muscle cells, Aqp4 for astrocytes, P2ry12/ Cx3cr1 for microglia, and Snap25/Syn1 for neurons). Cells from neuronal clusters were merged and re-clustered as above with 10 PCA components (estimated as significant by the JackStraw algorithm), yielding 6 initial clusters. Differential gene expression was carried out using Monocle2 (Trapnell et al., 2014). Only 3 clusters had 2-fold enriched genes (Clusters without 2-fold enriched genes were not considered distinct cell types, but instead a result of overclustering). Cells in these 3 clusters were used as a training set to classify the other cells using a random forest classifier (using the Seurat function ClassifyCells()). Bootstrapping by repeating this classification process 1000 times produced a metric for classification. Cells that were classified < 95% of the time to the same cluster were excluded. This final classification was used as input for differential gene expression using Monocle2.

Electrophysiological Analysis

Electrophysiological properties and ChR2-evoked EPSCs were performed using automated scripts written in MATLAB (https://github.com/bernardosabatini/physiologyAnalysis). Following the electrophysiology analysis white papers of the ABA we did not make *a priori* assumptions about the input resistance, resting potential, or minimal firing rate necessary to designate a cell as "healthy." Therefore, our final dataset includes neurons that, for example, do not fire any action potentials to injected current. Selection of neurons for inclusion was based on the series resistance. Tables containing the name of the cell, annotations about the position of the cell and conditions of the experiment were noted during the experiment including the start and stop sweeps to be analyzed which were then used to automatically retrieve and analyze data.

Intrinsic properties

Resting membrane potential was measured as the median of potentials during periods of the sweep that had no current injection. Membrane capacitance (Cm) and resistance (Rm) as well as series resistance (Rs) were measured in voltage-clamp mode by fitting a single exponential to the current evoked by a −5 or −10 mV voltage pulse. Rs was estimated from the peak of the exponential fit – i.e., $Rs = \Delta V/\Delta I(t = 0)$ with $t = 0$ being the start of the voltage step command. The steady-state current was used to calculate $Rm = \Delta V/\Delta I(t = \infty)$ - Rs. Cm is then calculated from the time constant of the fit tau = RsRmCm/(Rs+Rm). Action potentials were identified from peaks crossing 0 mV. Action potential threshold was determined from the voltage at the time corresponding to the peak of the second derivative of the voltage and maximum dV/dT was measured from the peak of the first derivative. Sag potentials were measured using a −100 pA current injection and quantified as the difference between the minimum voltage and the voltage at the end of the pulse.

EPSCs

Resting membrane properties were measured as above. To determine the amplitude of the EPSC and compare it to the amplitudes expected from chance fluctuations of the membrane potential (e.g., due to thermal and seal noise or spontaneous synaptic events), two 15 ms long periods were analyzed in each sweep. The first was a time window after the light pulse in which a genuine ChR2-evoked EPSC would be expected. In this window, the average current compared to baseline was calculated, as well as its peak deviation (positive for NMDA-receptor mediated currents at positive potentials and negative for AMPA-receptor mediated currents at rest). In addition, a "peri-peak" value was calculated from the average current in a time window (3 ms long) around the time of the peak deviation from rest in the average of all sweeps for the cell and that is reported in all plots as filled circles. Identical analyses were carried out in a time window occurring 50 or 100 ms before the light pulse to estimate baseline fluctuations for each parameter and these are reported as open circles in all plots. All measurements of AMPA-receptor mediated EPSCs were done at −70 mV. For NMDA-receptor mediated EPSCs, the reversal potential of the EPSC was found (typically at nominally +5-10 mV) and the cell was depolarized a further 20 mV, at which the measurement was made. No corrections were made for liquid junction potential (~8 mV).

DATA AND SOFTWARE AVAILABILITY

Data and software are available upon request or on Github (https://github.com/bernardosabatini/physiologyAnalysis). Table S1 gives a list of all the acronyms used in all the figures. Table S2.1 gives the data from experimental design shown in Figure 1A. Table S2.2 gives the full dataset for analysis done in Figure 6. Table S3 gives the results for the experiment shown in Figure S2C. Tables S4.1–S4.4 gives full genes list from the analysis done in Figure 3. Table S4.5 gives additional data from the experiment shown in Figures 3G–3K.

The accession number for the data files for RNA sequencing reported in this paper is GEO: GSE128393 and can be found at https://www.ncbi.nlm.nih.gov/geo/query/acc.cgi?acc=GSE128393.